



www.sciencemag.org/cgi/content/full/science.aat6141/DC1

## Supplementary Materials for

### **Reversible self-assembly of superstructured networks**

Ronit Freeman, Ming Han, Zaida Álvarez, Jacob A. Lewis, James R. Wester,  
Nicholas Stephanopoulos, Mark T. McClendon, Cheyenne Lynsky, Jacqueline M. Godbe,  
Hussain Sangji, Erik Luijten\*, Samuel I. Stupp\*

\*Corresponding author. Email: s-stupp@northwestern.edu (S.I.S.); luijten@northwestern.edu (E.L.)

Published 4 October 2018 on *Science* First Release  
DOI: 10.1126/science.aat6141

#### **This PDF file includes:**

Materials and Methods  
Figs. S1 to S40  
Tables S1 to S4  
Caption for movie S1  
References

#### **Other supplementary material for this manuscript includes:**

Movie S1

## Materials and Methods:

PA synthesis and purification: Peptides were synthesized on solid support using a rink amide MBHA resin (100-200 mesh,  $0.55 \text{ mmol g}^{-1}$ ) using standard fluorenylmethyloxycarbonyl (fmoc) procedures. The unnatural amino acids azidolysine (denoted  $K^{az}$ ) and Fmoc-NH-OEG<sub>x</sub>-(CH<sub>2</sub>)-COOH (denoted PEG<sub>x</sub>) were incorporated as indicated. Following synthesis, the peptides were cleaved from the resin using a 95:2.5:2.5 mixture of trifluoroacetic acid:triisopropyl silane:water, and precipitated using cold diethyl ether. The peptides were purified using reverse phase HPLC (Varian Prostar 363, Jupiter 10u Proteo 90A column) using a water/acetonitrile gradient (2-100% acetonitrile over 60 min) with 0.1% ammonium hydroxide. Purified peptides were lyophilized and stored at  $-20 \text{ }^{\circ}\text{C}$ . The purity of the peptides was confirmed by electrospray ionization mass spectrometry in positive mode (ESI-MS, Agilent 6510 Q-TOF).

DNA-PA synthesis, purification, and quantification: Oligonucleotides modified with a terminal amine were purchased from Integrated DNA technologies and dissolved to 1 mM in 100 mM phosphate buffer, pH 8.3. Dibenzocyclooctyne-sulfo-*N*-hydroxysuccinimidyl ester (DIBAC-sulfo-NHS, Sigma-Aldrich) was added to the DNA solution as a 100 mM solution in DMSO to 5 equivalents. The mixture was incubated at room temperature for 2 hours under vigorous shaking, after which the solvent was exchanged to fresh 100 mM phosphate buffer, pH 8.3, using an Amicon Ultra-0.5 filter unit, 3 kDa, 5 eq DIBAC were added as before, and the pH was adjusted to 8.3 by adding 1 M sodium hydroxide as necessary. The mixture was incubated at  $4^{\circ}\text{C}$  overnight under vigorous shaking after which excess DIBAC was removed using an ultracentrifuge filtration unit. To this solution were added two equivalents of the azide-modified peptide amphiphile dissolved in 0.1 % ammonium hydroxide to 1 mM. Sodium chloride was added to a final concentration of 100 mM and the solution was gently agitated overnight. Following conjugation, the solvent was once again exchanged using an ultracentrifuge filtration unit to 50 mM triethylammonium acetate buffer (TEAA), pH 7, and concentrated to  $\sim 1 \text{ mM}$  DNA.

The DNA-PA was purified by reverse-phase HPLC (Agilent 1260 Infinity, DIKMA Inspire C18 column ( $5 \mu\text{m}$ ,  $250 \times 4.6 \text{ mm}$ ) with a gradient of organic buffer B (90% acetonitrile in water, +50 mM TEAA, pH 7) in water +50 mM TEAA, pH 7 (buffer A, using a 5-50% B gradient over 30 min. Absorbance at 260 nm was monitored, with unmodified DNA eluting at  $\sim 12 \text{ min}$ , and P-DNA conjugates approximately 21-26 min. Fractions containing DNA-PA were concentrated using ultracentrifuge filtration units and the resulting DNA concentration was quantified by UV-vis absorbance at 260 nm, followed by lyophilization.

The PNA-PA was purchased from PNABio.

Rheology: Rheological experiments were performed using Anton Paar MCR 302 rheometer with a 25 mm diameter  $2^{\circ}$  angle cone-plate oscillating geometry. Prior to testing 100  $\mu\text{l}$  PA solution

was placed on the stage while 100  $\mu\text{l}$  gelling solution (150 mM sodium chloride, 25 mM calcium chloride, 3 mM potassium chloride) was placed on the fixture. The fixture was lowered to the stage mixing the PA and the gelling solution. The temperature was maintained at 37  $^{\circ}\text{C}$  and the gap was sealed with mineral oil to prevent evaporation. A 15-minute equilibration period at 0.1% oscillatory strain and  $10\text{ s}^{-1}$  oscillatory frequency preceded further testing. Next, a frequency sweep was performed (100 to  $1\text{ s}^{-1}$ ) with the strain held at 0.1%. Finally, a strain sweep was performed from 0.1% to 100% strain at constant  $10\text{ s}^{-1}$  frequency.

Scanning electron microscopy: For scanning electron microscopy, polystyrene sponges were coated in PA solution by soaking. The PA-coated sponges were then incubated in gelling solution and incubated for 1 hour at room temperature. PA coated coverslips were fixed with a solution of 2.5% glutaraldehyde, 2% paraformaldehyde in PBS for 30 minutes at room temperature. All samples were dehydrated by exposure to a graded series of water-ethanol mixtures. Once in 100% ethanol, the samples were dried at the critical point of  $\text{CO}_2$  using a critical point dryer (Tousimis Samdri-795), and dried samples were coated with 14 nm of osmium using an osmium plasma coater (Filgen, OPC-60A). Imaging was performed using a LEO Gemini 1525 field emission scanning electron microscope at 20 kV accelerating voltage.

Transmission electron microscopy: For transmission electron microscopy, PA samples were diluted 10 times in distilled water, cast on carbon-film-coated 300-mesh copper grids (electron microscopy sciences) for 5 minutes, and then wicked off the grid. The grids were rinsed twice with sterile water, stained twice for 20 seconds with 2% uranyl acetate in water, and then rinsed twice more. Imaging was performed on an FEI Tecnai Spirit G2 at an accelerating voltage of 80 kV.

Small-angle x-ray scattering: Experiments were performed at the DuPont-Northwestern-Dow Collaborative Access Team Synchrotron Research Center at the Advanced Photon Source, Argonne National Laboratory. The instrument comprised a double-crystal monochromator to select 17 keV x-rays with a CCD camera placed 245 cm behind the sample to record scattering intensity. Samples were measured in a 1.5 mm quartz capillary exposed to x-ray for 0.5 to 5 seconds. Scattering intensity was plotted against the wave vector  $q = (4\pi/d)\sin(\theta/2)$  where  $d = 2\pi/q$ . The two-dimensional scattering images were averaged using azimuthal integration and plotted on a relative scale as a function of the wave vector, following background subtraction of buffer-only controls.

AFM nanoindentation: The Young's modulus of coatings was measured by Atomic Force Microscopy (AFM, Dimension Icon, Bruker Corp). An AFM tip with a 20-nm tip radius (MLCT-Bio-E, Bruker Corp) was used to indent coatings in Peakforce Force Tapping mode at 1 KHz with an amplitude of 100 nm in 2 mM calcium solution bath. DNA-PA bundles were identified by their morphology in the topographic image, and force curves on the bundles were

selected for analysis. Individual force curves were fit with the linearized Hertz model with an indentation depth of 10-15 nanometers.

Animals: All animal housing and procedures were performed in accordance with the Public Health Service Policy on Humane Care and Use of Laboratory Animals and all procedures were approved by the Northwestern University Institutional Animal Care and Use Committee.

Primary Cultures: Glial cells were derived from the cerebral cortex of newborn mice (P0), as described elsewhere (27). Briefly, cerebral cortices were dissected free of meninges in dissection buffer (PBS 0.6% glucose (Sigma-Aldrich), 0.3% BSA (Sigma-Aldrich)) and digested with trypsin (Biological Industries) and DNase I (Sigma-Aldrich) for 10 min at 37 °C. The tissue was dissociated in Dulbecco's Modified Eagle Medium (DMEM, Biological Industries), 10% normal horse serum (NHS, GIBCO), 1% penicillin-streptomycin (Pen-Strep, Biological Industries) and 2 mM L-glutamine (Biological Industries). After centrifugation and resuspension, cells were plated and grown to confluence at 37 °C, 5% CO<sub>2</sub> (approximately 25-30 days in vitro (div)). All experiments were performed using glial cells from the first passage (Ps1).

Passage 1 (Ps1) cells were cultured at a density of  $1 \times 10^5$  cells/cm<sup>2</sup> for 5 or 10 days in vitro (div) in DMEM, 1% Pen-Strep, and 2 mM L-glutamine on non-coated culture plastic (for Western blotting) or glass (for immunocytochemistry, cell survival and ROS assay). The cell composition and biochemical characterization of control and reference glial conditions have been described previously (28).

Glial cell culture and dynamic modulation on PA-DNA platforms: Glial cells were plated on poly D-lysine surfaces coated with various PA hydrogels: E3 PA (gelled with calcium), DNA-PA Individual fibers (IF), DNA-PA Bundled fibers (BF) for 5 div. Then, a solution containing the invader or anti-invader strands (10 μM) was added to the media and the cells were cultured for an additional 5 div. As control conditions, astrocytes were cultured on glass coverslips with or without dibutyl cyclic adenosine monophosphate (dAMPc) at 500 mM (Sigma-Aldrich) (28).

Western blot: For Western blot analysis, protein extracts were obtained from primary cultures after 5 or 10 div, and total protein extracts were separated by SDS-polyacrylamide gel electrophoresis and electro-transferred to a nitrocellulose membrane (Bio-Rad). Membranes were blocked with 5% bovine serum albumin (BSA, Sigma-Aldrich) and incubated first with primary antibodies overnight at 4°C, and then with their corresponding secondary HRP-conjugated antibodies (1:3000; Santa Cruz Biotechnology). Protein signals were detected by the ECL chemiluminescent system (Azure Biosystems). Densitometry analysis, standardized to Actin as a control for protein loading, was performed with ImageJ software (National Institutes of Health, USA). The analyses were done in 3 independent experiments with 3 replicates per condition.

Immunocytochemistry: For immunofluorescence, fixed primary cultures were incubated with primary antibodies overnight at 4°C, and then with their appropriate Alexa 488 or Alexa 555 secondary antibodies (1:500, ThermoFisher). DAPI (1:500, ThermoFisher) was used to stain nuclei. Finally, the preparations were cover-slipped Immu-Mount (Thermo Scientific) for imaging. The following primary antibodies were used for Western blot and/or Immunocytochemistry; rabbit anti-GFAP (mature and reactive glial marker, 1:500-1:8000, Dako), mouse anti-Vimentin (neuronal marker 1:10000, Abcam) and mouse anti-Actin (1:1000, Cell signaling).

Cell viability: For cell viability experiments, media was exchanged with PBS containing 2  $\mu$ M calcein-AM (Life Technologies) and 100 ng/ml propidium iodide (Sigma Aldrich) for 20 min at 37°C. The cells were then rinsed with PBS and imaged with a Nikon A1R confocal laser-scanning microscope with GaAsP detectors. Live and dead cells were counted using the Cell Counter plug-in for ImageJ.

Cell proliferation analysis. For astrocytes proliferation assay, 2  $\mu$ M of the thymidine analog 5-ethynyl-2'-deoxyuridine (EdU, Thermo Fisher) was incorporated into the culture medium for 24 hours. Cells were fixed at the indicated time points (24h, 5div and 10div) in 4% paraformaldehyde (PFA) for 15 min at room temperature (RT). After fixation samples were washed in PBS twice and then stained with EdU staining cocktail containing 11 mM CuSO<sub>4</sub> (from 50 mM stock) and 1  $\mu$ g/ml of Alexa Fluor-488 azide (from 0.5 mg/ml, Thermo Fisher) for 30 minutes at RT in the dark. The staining cocktail was then removed, and cells were washed with PBS. Then, astrocytes were used for counterstained with 4', 6-diamidino-2-phenylindole (DAPI, Thermo Fisher) at 5  $\mu$ g/ml in PBS for 20 min at RT. The cells were washed with PBS and mounted with Immu-Mount (Fisher Scientific). Fluorescent images were taken using a Nikon Ti2 Widefield Microscope. Image files were imported into Fiji software and the “analyze particles” and “cell counter” functions were used to measure the total number of nuclei (DAPI positive) and proliferative nuclei (EdU positive). The number of EdU-positive cells was divided by that of DAPI-positive cells to obtain the percentage.

Reactive oxygen species (ROS): For the detection of ROS in astroglial cells, media was exchanged with PBS containing CellROX® Reagent (Life Technologies) at a final concentration of 5  $\mu$ M for 30 minutes at 37°C. The CellROX reagent was then removed and cells were washed with PBS and counterstained with Hoechst (1:1000, Life Technologies) for 20 min at RT. The cells were then rinsed with PBS and imaged with a Nikon A1R confocal laser-scanning microscope with GaAsP detectors. Image files were imported into Fiji software and the “analyze particles” and “cell counter” functions were used to measure the number of cells (Hoechst positive) and ROS cells (ROS positive). The number of ROS-positive cells was divided by that of Hoechst-positive cells to obtain the percentage.

Imaging/analysis of cells: Fluorescent preparations were viewed and micrographs were captured with a Nikon A1R confocal laser-scanning microscope with GaAsP detectors or a Nikon Ti2 Widefield Microscope. Images were assembled in Adobe Photoshop (v. 7.0), with adjustments for contrast, brightness, and color balance to obtain optimum visual reproduction of data. The analyses were performed using ImageJ software (National Institutes of Health, USA).

Simulation procedures: Coarse-grained molecular dynamics (MD) simulations were performed to study the generic behavior of fiber intertwining and the underlying mechanism of bundle formation.

Each fiber consisted of a cylindrical peptide-amphiphile (PA) backbone and nucleotide side chains (Fig. S5). We modeled the fiber backbone as a chain of overlapping spheres with diameter  $\sigma_c = 12.6$  nm, the width of a PA fiber (29), and center-to-center distance  $d_c = 0.1 \sigma_c = 1.26$  nm. Each backbone sphere consisted of a group of 23 PA monomers and was grafted with up to  $n_{\max} = 23$  DNA or PNA side chains (corresponding to 100% nucleotide coverage). The side chains were coarse-grained into bead chains of diameter  $\sigma_s = 0.1 \sigma_c = 1.26$  nm (single-stranded DNA width). Each bead represented 5 nucleotide bases, had a center-to-center distance  $d_s = 0.135 \sigma_c = 1.7$  nm ( $5 \times$  nucleoside length), and either carried a charge  $-5e$  or was neutral, depending on the nucleotide type (DNA or PNA).

Bead connections were modeled via harmonic bond potentials,

$$U_{\text{bond}}(r) = k_{\text{bond}} (r - r_0)^2,$$

with minimum-energy bond length  $r_0$  and strength  $k_{\text{bond}}$ , as listed in Table S4. Strong permanent bonds (black lines in Fig. S5) were utilized to preserve the desired bead distances.

To implement the desired fiber stiffness, a harmonic angle potential was introduced between every two adjacent bonds,

$$U_{\text{angle}}(\theta) = k_{\text{angle}} (\theta - \theta_0)^2,$$

with equilibrium angle  $\theta_0$  and strength  $k_{\text{angle}}$ , as listed in Table S3. The backbone had  $k_{\text{angle}} = 10^4 k_B T / \text{rad}^2$ , rendering the persistence length of individual fiber  $L_p \approx 25$   $\mu\text{m}$  in experiment. The side chain had  $k_{\text{angle}} = 0.3 k_B T / \text{rad}^2$ , yielding the persistence length of a single-stranded DNA  $L_p \approx 1$  nm).

Furthermore, we employed a purely repulsive shifted-truncated Lennard-Jones interactions to represent excluded-volume effects,

$$U_{\text{STLJ}}(r) = 4\epsilon \left[ \left( \frac{\sigma}{r} \right)^{12} - \left( \frac{\sigma}{r} \right)^6 + \frac{1}{4} \right],$$

with strength  $\varepsilon = k_B T$ , minimum bead distance  $\sigma$  ( $=\sigma_c$ ,  $\sigma_s$ , or  $(\sigma_c + \sigma_s)/2$  for a BB, DD, or BD bead pair, respectively), and cutoff  $r_c = 2^{1/6} \sigma$ . A Yukawa potential was utilized to account for screened electrostatic interactions,

$$U_{\text{Yukawa}}(r) = \frac{q_i q_j}{4\pi\epsilon_0 \epsilon_{\text{water}} r} \exp(-r / \lambda_D),$$

where  $q_i$  is the charge valence,  $\epsilon_0$  the vacuum permittivity,  $\epsilon_{\text{water}}$  the relative permittivity of water, and  $\lambda_D$  the Debye length, chosen to be 1 nm to reflect an ion concentration of  $\sim 100$  mM.

To mimic the hybridization process, we exploited the concept of dynamic bonding. When two complementary nucleotide beads were closer than  $s_f = 0.16\sigma_c = 2$  nm (double-stranded DNA width) and furthermore were not part of another hybridized pair, a weak temporary bond was created to join them. This dynamic bond would break when the bead distance became larger than  $s_b = 0.24\sigma_c = 3$  nm. The breakup required an energetic cost of  $9k_B T$ , corresponding to the hybridization energy of 5 nucleotide pairs (30). Hybridization also affects the stiffness of nucleotide strands. To account for this, we increased the strength of the angle potential for two hybridized side chains to  $k_{\text{angle}} = 7.5 k_B T / \text{rad}^2$ , corresponding to the persistence length of double-stranded DNA,  $L_p \approx 50$  nm.

Intertwining of two complementary fibers: We simulated the intertwining process of two 3  $\mu\text{m}$ -long fibers, one grafted with DNAs while the other was grafted with complementary PNAs. Without loss of generality, the two fibers were initially placed at an arbitrary contact angle. We systematically explored the influence of contact angle, nucleotide coverage, DNA length, and fiber stiffness on the intertwining behavior.

Bundle formation in a gel system: We investigated the bundle formation in a gel system. Given the supramolecular nature of the fibers, we permitted the exchange of DNA strands among the fibers. To study the role of this DNA exchange in the bundle formation, we first allowed DNA side chains to detach from (and rejoin with) fiber backbones via dynamic bonding. Using this approach, we studied the influences of intra-fiber energy  $E_{\text{intra}}$  (PA hydrophobicity and  $\beta$ -sheet formation) and inter-fiber energy  $E_{\text{inter}}$  (DNA hybridization) on the bundle growth.

A cubic domain of side length  $L = 1.5 \mu\text{m}$  was employed, containing more than 500 fibers of length  $l = 1 \mu\text{m}$  and with periodic boundary conditions applied in all three dimensions. The simulations started from configurations with random fiber arrangements.

The simulations for both the intertwining and the bundling events ran for more than  $10^9$  time steps with step size  $dt = 10^{-4} \tau$ , where  $\tau = (m_c \sigma_c^2 / k_B T)^{1/2} \approx 10$  ns is the time unit (where  $m_c$  is the mass of the backbone bead).

## Discussion:

### Discussion S1: Assessment of the interaction energy scales in experiment

DNA hybridization ( $E_{\text{inter}}$ ) and the peptide hydrophobic binding energy ( $E_{\text{intra}}$ ) play a role in the assembly process. In order to achieve bundle formation, the lower of these two must be in the interaction range of 5-10  $k_B T$ , and both can be controlled via molecular design.

For the assemblies in Fig. 1, the DNA sequences that we employed yielded an inter-fiber energy of 64  $k_B T$ , according to the calculation by OligoCalc (31). In view of this strong hybridization, we conclude that bundling was controlled by the hydrophobic interaction of the peptide amphiphiles (PAs). To estimate this intra-fiber energy, we employed a coarse-grained approach (32) based upon the Martini force field (33, 34). The PA sequence was treated as a linear chain with 3 C1-type beads (the hydrophobic tail) concatenated by 9 Nda-type beads (the amino acid sequence), embedded in an aqueous environment modeled with P4-type water molecules. We assumed that each bead on average interacted with 6 nearest neighbors. When a PA detached from a fiber, it became exposed to the water environment. This led to the breakup of 6.5 C1-C1, 18 Nda-Nda and 24.5 P4-P4 bonds, accompanied by the formation of 13 C1-P4 and 36 Nda-P4 bonds, yielding a net enthalpy change of 22.5  $k_B T$ . Moreover, approximating the morphology change of the PA upon detachment as a semiflexible coil, we estimated the entropy gain as 16.5  $k_B$ . Thus, the intra-fiber energy was approximately 6  $k_B T$ , in good agreement with the range of 5-10  $k_B T$  predicted using our more coarse-grained model. This properly tuned energy explains the emergence of big bundles.

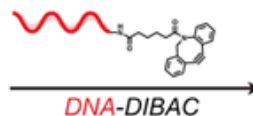
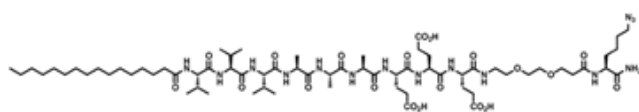
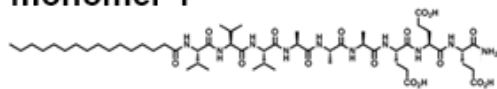
For the assemblies in Fig. S14-15, a shorter PA sequence was employed. Using the same coarse-grained approach as above, we could treat it as a chain of 2 C1-type beads (the hydrophobic tail) concatenated by 9 Nda-type beads (the amino acid sequence). In this case, the detachment of a PA from the fiber led to the breakup of 4.5 C1-C1, 18 Nda-Nda and 22.5 P4-P4 bonds, along with the formation of 9 C1-P4 and 36 Nda-P4 bonds, yielding a net enthalpy change of 18.9  $k_B T$ . Moreover, the morphology change of the PA gave rise to an entropy gain of 15  $k_B T$ . Therefore, the intra-fiber energy was approximately 3.9  $k_B T$ , below the threshold of 5  $k_B T$  predicted by the simulation. Indeed, it was so weak that the assembly of pure PA monomers resulted in a mixture of fibers and micelles (Fig. S15A) while the co-assembly with DNA-containing monomers resulted in no bundles (Fig. S15B).



## Figures:

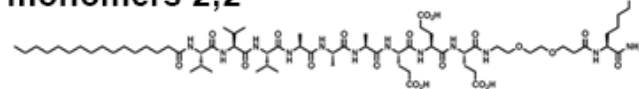
### (1) Click chemistry synthesis of DNA-PA

#### monomer 1

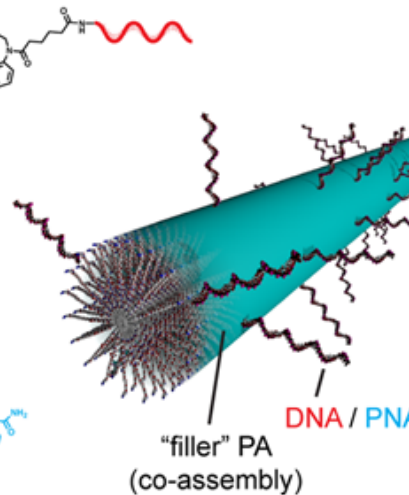


$C_{16}$ -V3A3E3-(PEG)<sub>2</sub>-azK  
(synthesized on solid-phase)

#### monomers 2;2'

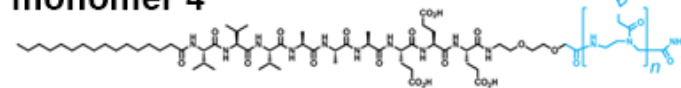


DNA-PA conjugate  
(purified by HPLC)



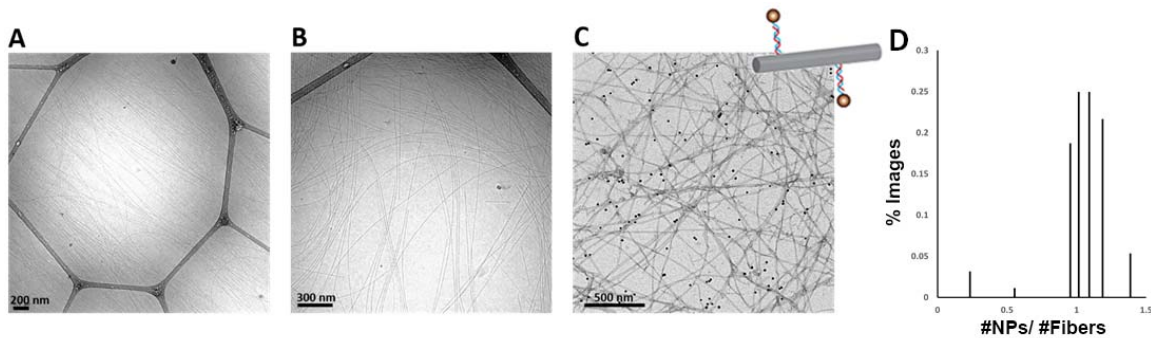
### (2) Solid-phase synthesis of PNA-PA

#### monomer 4

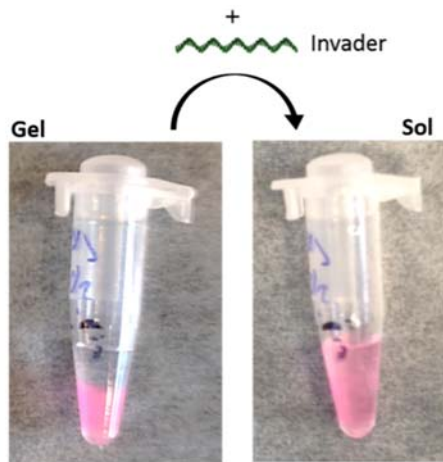


PNA-PA conjugate

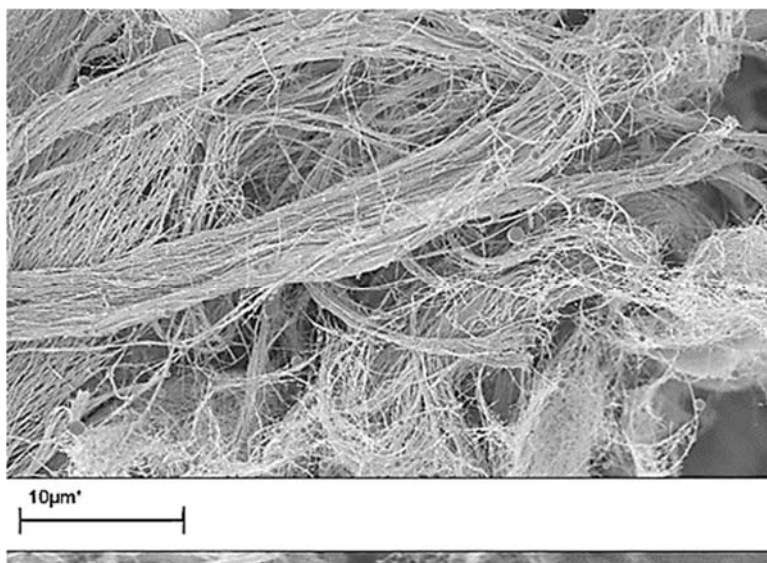
**Figure S1: Synthesis of oligonucleotide-peptide amphiphiles. (1) Synthesis of DNA-PA (2) Synthesis of PNA-PA.**



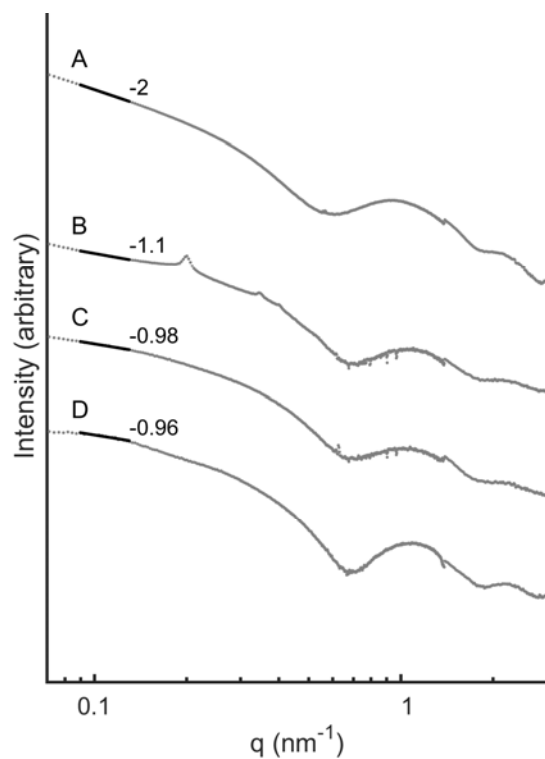
**Figure S2: TEM images of the self-assembled structures formed by various co-assemblies of DNA-PA.** Cryo-TEM images of the DNA-PA obtained by (A) mixing monomers **1** and **2** in a 1:0.01 molar ratio and (B) mixing monomers **1** and **2** in a 1:0.1 molar ratio. (C) TEM image of the DNA-PA obtained by mixing monomers **1** and **2** in a 1:0.1 molar ratio in the presence of a DNA complementary strand modified with gold nanoparticles (as shown in inset). (D) Ratio between number of particles (NPs) to fibers over 10 images divided to 3 by 3 frames. Graph shows that most frames (~90%) have a similar ratio between particles to fibers, suggesting a stochastic distribution of particles along the fibers.



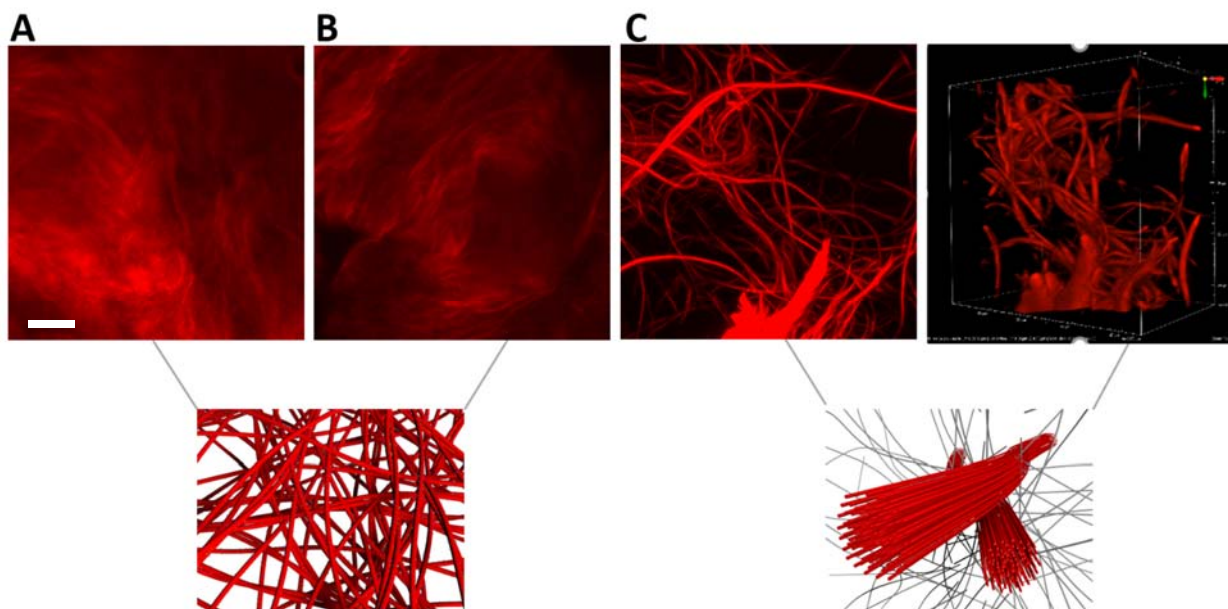
**Figure S3: Reversible Gelation.** Gel (left panel) vs. sol (right panel) after addition of the invader strand.



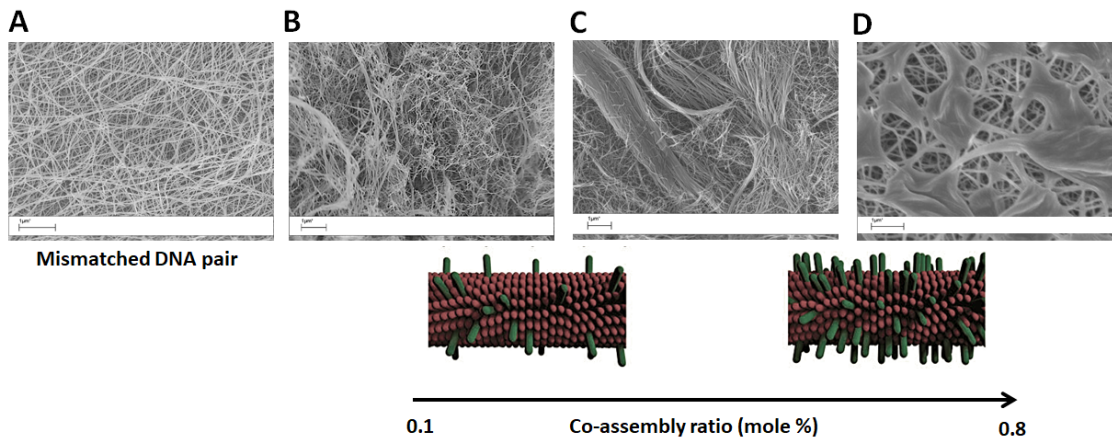
**Figure S4: SEM image of bundles formed by mixing all monomers together simultaneously.** Adding all components at once ( $1/2$ ;  $1/2'$ ) resulted in similar phase separation containing bundles and thinner filaments.



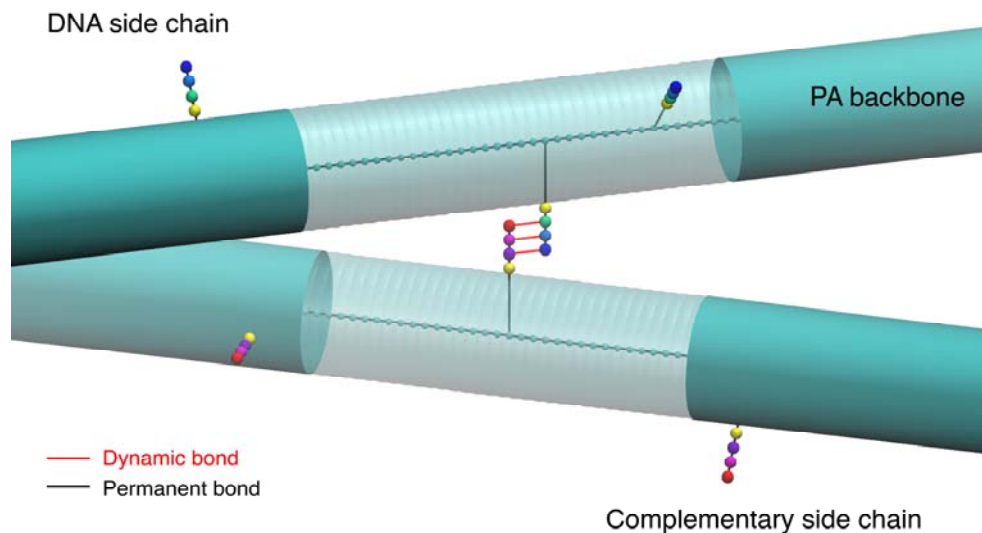
**Figure S5: SAXS scattering patterns of:** (A) DNA cross-linking after mixing and annealing solutions containing fibers with monomers **2** and **2'**. (B) monomer **2** only, (C) monomer **2'** only, (D) backbone PA only (monomer **1**). Higher slope on the low- $q$  regions indicates formation of higher-order structures.



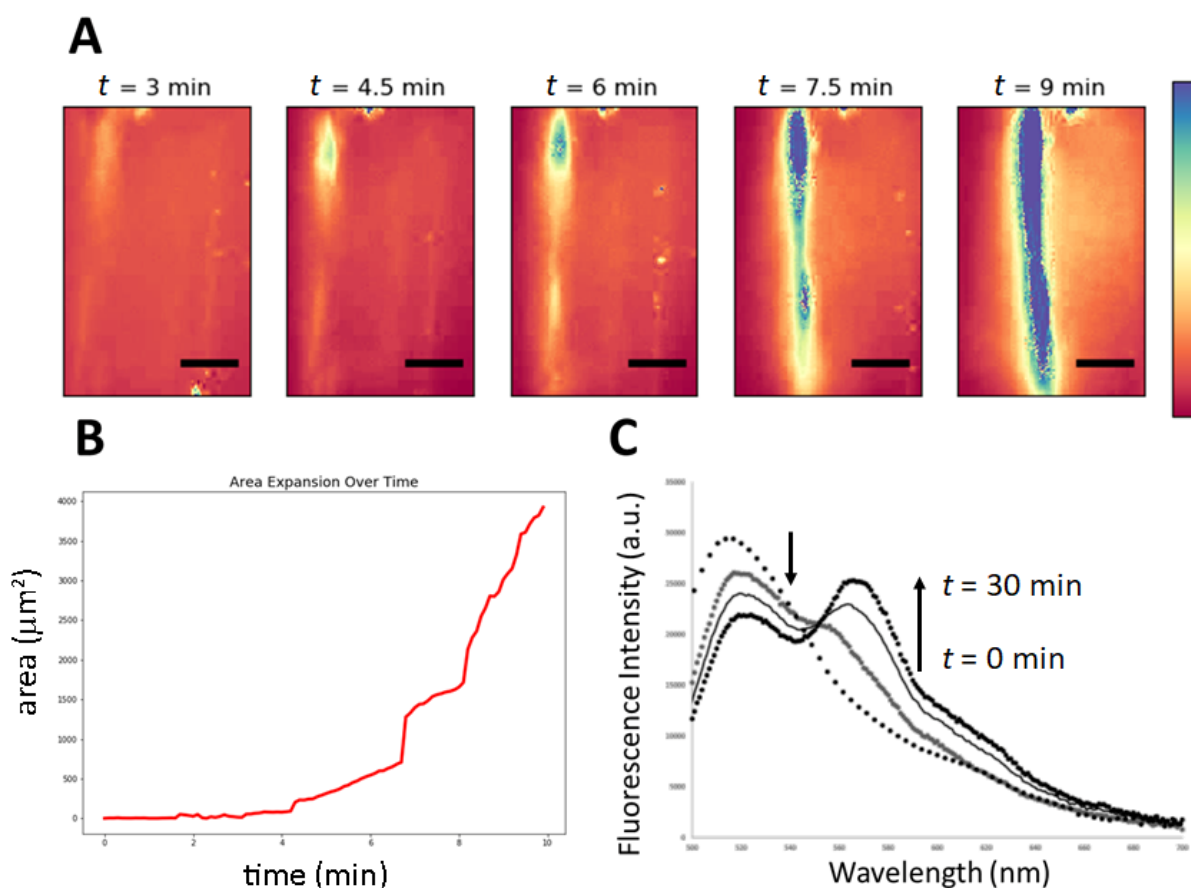
**Figure S6: Confocal images of DNA-PA gels.** (A-B) Confocal microscopy images of electrostatic cross-linking (addition of calcium chloride) of solutions containing fibers with either (A) monomer **2** or (B) monomer **2'**. (C) Confocal microscopy image (left) and reconstruction image of section of hydrogel (right) formed upon DNA cross-linking after mixing solutions containing fibers with monomers **2** and **2'**. Images below the panels are schematic illustrations of the corresponding fiber structures. In all images the oligonucleotides are labeled with a fluorescent dye (Cy3) to probe their distribution in the hydrogel. Scale bar: 10  $\mu\text{m}$  and relevant to all images.



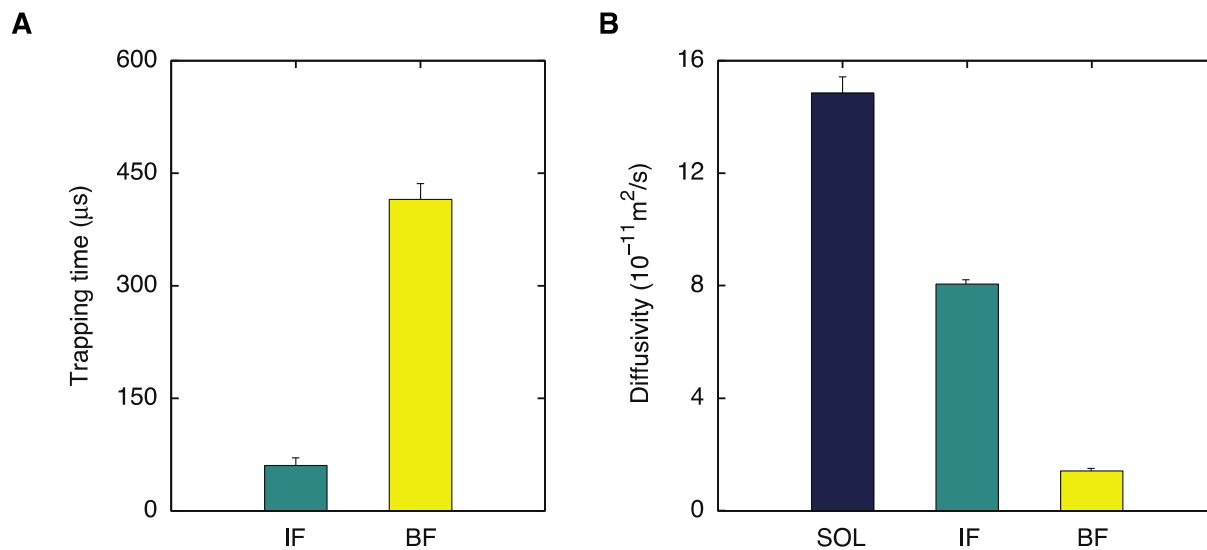
**Figure S7: SEM micrographs of:** (A) Fibers containing noncomplementary oligonucleotides (monomer 2 and scrambled monomer 2'). Non-complementary oligonucleotides did not yield bundled structures. (B-D) DNA cross-linking after mixing solutions containing fibers with monomers 2 and 2' at DNA coverage of (B) 0.1 mole % (C) 0.4 mole % (D) 0.8 mole %. The intermediate DNA coverage (0.4 mole%) resulted in larger bundles than for 0.1% and 0.8%.



**Figure S8. Schematics of the bead-spring model.** Each fiber consisted of a cylindrical backbone randomly grafted with either DNA or PNA. The backbone was modeled as a chain of overlapping spheres with center-to-center distance much smaller than their radius, as illustrated in the transparent region. The side chains were linked to the centers of the backbone spheres. When two complementary side chains met, temporary bonds (red lines) were formed, mimicking the hybridization process.

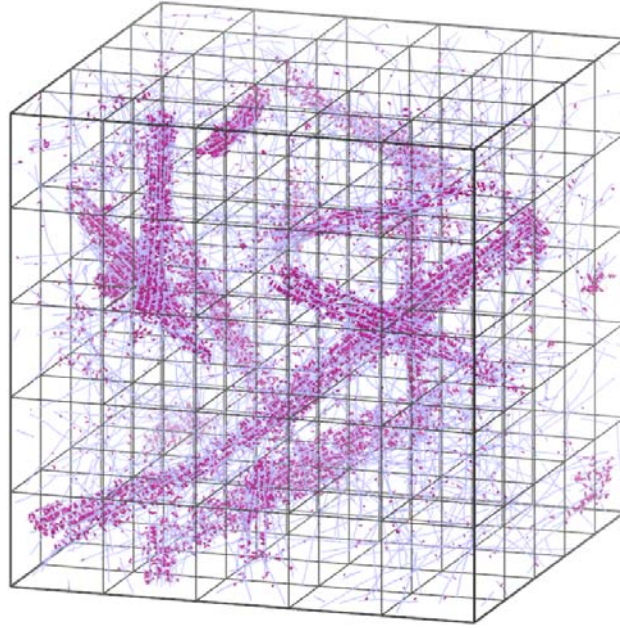


**Figure S9: Kinetics of bundle formation and molecular exchange.** (A) Time-lapse monitoring the growth of a bundle using a fluorescently tagged monomer (Cy3-modified monomers **2** and **2'**). The frames are colored as a heatmap to better illustrate the difference in color of the bundled regions. Scale bars are  $20 \mu\text{m}$ . (B) Kinetics of bundle growth over time quantified by intensity of the red color channel per pixel at each frame of the time-lapse. All data analysis was completed using the matplotlib, sci-kit image, and numpy Python libraries. (C) The timescale of hybridization and molecular exchange was measured using FRET kinetic experiments. Two sets of PA nanofibers were pre-assembled separately from a mixture of non-labeled PAs with either Fluorescein, FAM-monomer **2** (0.1%) or Cyanine, Cy3-monomer **2'** (0.1%). The two solutions were mixed at a final PA concentration of  $0.5 \text{ mM}$  and the fluorescence-emission spectra were recorded over time (spectra shown in 10-minute intervals) at the excitation wavelength of FAM ( $450 \text{ nm}$ ), at which direct excitation of Cy3 is negligible. After 30 minutes considerable FRET emission of the acceptor dye (Cy3) can be seen, providing evidence for molecular exchange between nanofibers.

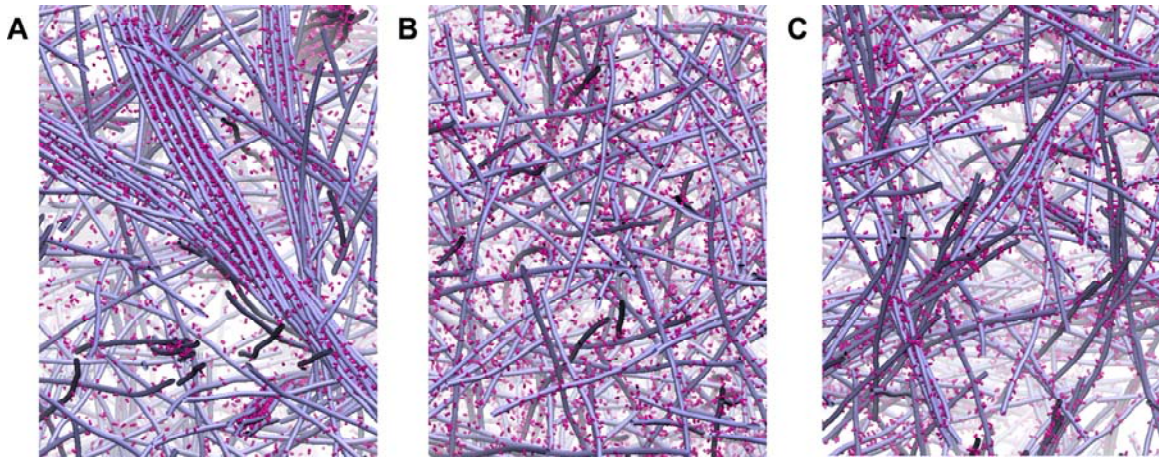


**Figure S10: Dynamics of DNA-containing monomers.** (A) Trapping time, defined as the time span between the entrance and departure of a monomer from a region. On average, a DNA-containing monomer was trapped on a bundled fiber (BF) seven times longer than on an individual fiber (IF). (B) Diffusivity. Compared to free DNA in solution (SOL), DNA-containing monomers on IFs and BFs had a diffusivity that was suppressed by 50% and 90%, respectively.

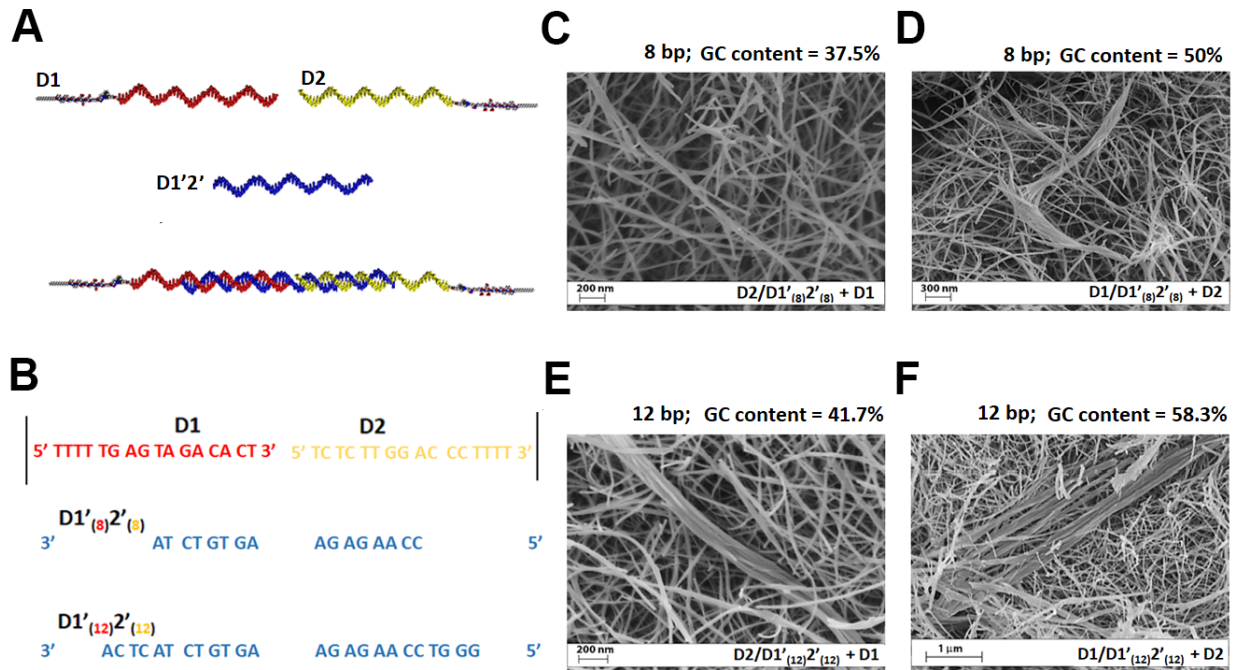




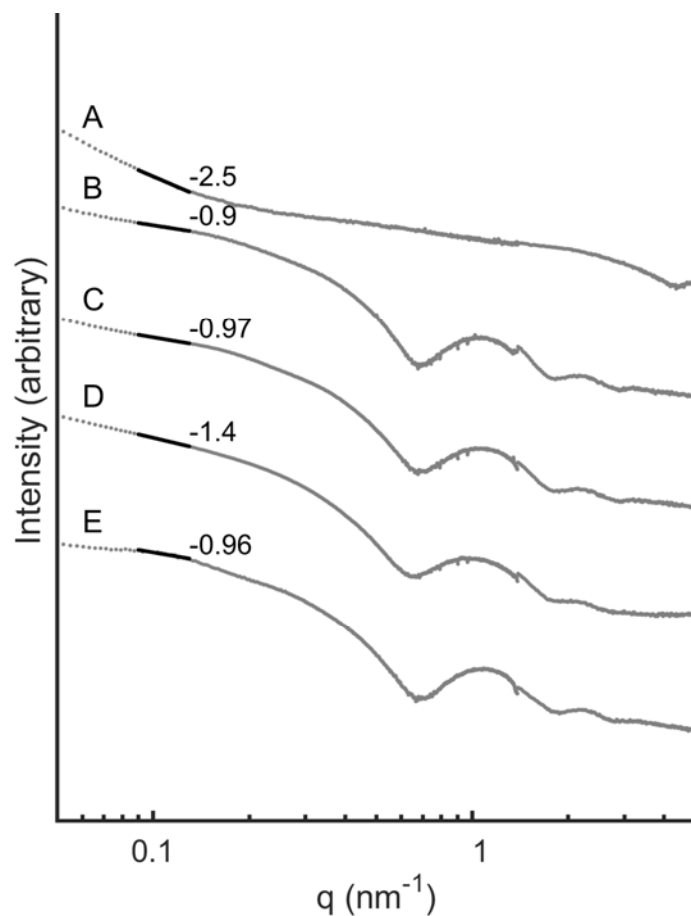
**Figure S11: Calculation of the bundle growth rate.** We designed a global order parameter  $m$  to quantify the emergence of large bundles owing to large-scale DNA redistribution. The entire system was meshed with a 3D grid. For clarity, a  $5 \times 5 \times 5$  grid is shown; the actual calculations employed a  $10 \times 10 \times 10$  grid. For each cube  $i$ , we calculated the DNA concentration  $c_{\text{DNA}}(i)$ , the fiber density  $\rho_{\text{fiber}}(i)$ , and the liquid-crystal order parameter of the fibers,  $s_{\text{fiber}}(i)$ .  $c_{\text{DNA}}(i)$  represents the spatial distribution of DNA, whereas  $\rho_{\text{fiber}}(i) \cdot s_{\text{fiber}}(i)$  quantifies local fiber bundling. We used their correlation to derive  $m = \langle c_{\text{DNA}}(i) \cdot \rho_{\text{fiber}}(i) \cdot s_{\text{fiber}}(i) \rangle_i / \langle c_{\text{DNA}}(i) \rangle_i \cdot \langle \rho_{\text{fiber}}(i) \cdot s_{\text{fiber}}(i) \rangle_i$ , where  $\langle \dots \rangle_i$  stands for the average over cube  $i$ . The bundle growth rate was calculated as  $dm/dt$ . We explored its dependence on intra- and inter-fiber energies, as shown in Fig. 1 in the main text.



**Figure S12: Influence of interaction energies on gel structures.** (A) Emergence of large bundles at an intra-fiber interaction  $E_{\text{intra}} = 8 k_B T$  and hybridization energy  $E_{\text{inter}} = 8 k_B T$ . The moderate intrafiber interaction allowed large-scale redistribution of DNA-containing monomers, which promoted bundle formation among fibers. These bundles then are held together by the sufficiently strong hybridization energy. (B) Random network at  $E_{\text{intra}} = 8 k_B T$  and  $E_{\text{inter}} = 2 k_B T$ . With a weak inter-fiber interaction, emergent bundle cannot be sustained. (C) Weak bundling at  $E_{\text{intra}} = 15 k_B T$  and  $E_{\text{inter}} = 8 k_B T$ . Here the relatively strong intra-fiber interaction suppressed redistribution of DNA, so that any bundle formation had to rely on rearrangement of the fibers. The DNA rehybridization required for that was permitted by the moderate inter-fiber energy. As a result, small bundles formed. All systems shown here had 0.4% DNA coverage. The order parameter quantifying the extent of bundling (defined in fig. S10) was 0.51, 0, and 0.09 for panels A, B, and C, respectively.

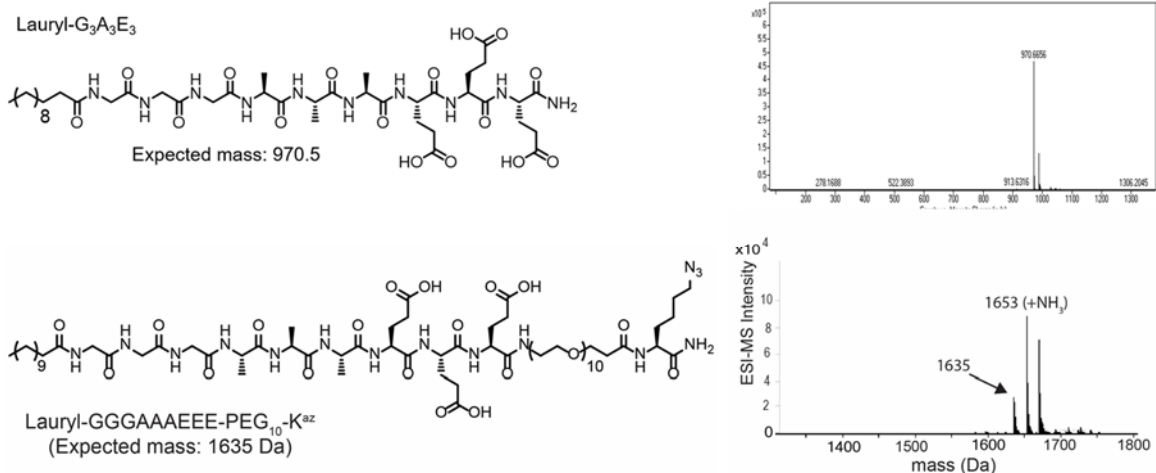


**Figure S13: Effect of DNA length and GC content on the formation of bundles:** (A) Molecular graphics illustrations of DNA monomers and their interactions. The crosslinking strand (**D1'2'**) bridges the two DNA-PA monomers (**D1**; **D2**). (B) Sequences of the monomers. The crosslinkers (of various lengths) consisted of 2 domains, one complementary to D1 and the other to D2. These two domains varied in the GC content and stability of the resulting duplex. (C-F) SEM micrographs of DNA-crosslinked gels formed by (C) pre-mixing of D2 and short crosslinker after addition of D1, (D) pre-mixing of D1 and short crosslinker after addition of D2, (E) pre-mixing of D2 and long crosslinker after addition of D1, and (F) pre-mixing of D1 and long crosslinker after addition of D2. Longer complementary domains and higher GC content stabilized the formation of larger bundles. According to OligoCalc (31), the hybridization energies involved in panels C-F were 8.9  $k_B T$ , 9.8  $k_B T$ , 19.4  $k_B T$ , and 22.3  $k_B T$ , respectively. The inter-fiber energy for the 8-base sequences with GC content 37.5% (panel C) and 50% (panel D) was so weak that it resulted in only weak bundling (mean bundle diameters correspond to  $43 \pm 6$  nm for C and  $121 \pm 35$  nm for D). In contrast, the inter-fiber energy in panels E-F (12-base sequences with GC content 41.7% and 58.3%, respectively) was strong enough to result in the formation of larger bundles (mean bundle diameters correspond to  $184 \pm 27$  nm for E and  $561 \pm 78$  nm for F). The increased bundling in panel F compared to panel E confirms that bundle formation can be enhanced not only by increasing DNA length, but also by increasing GC content. Quantification of bundle diameters utilized a minimum of 10 randomly selected images (taken from two independent batches) for each system.

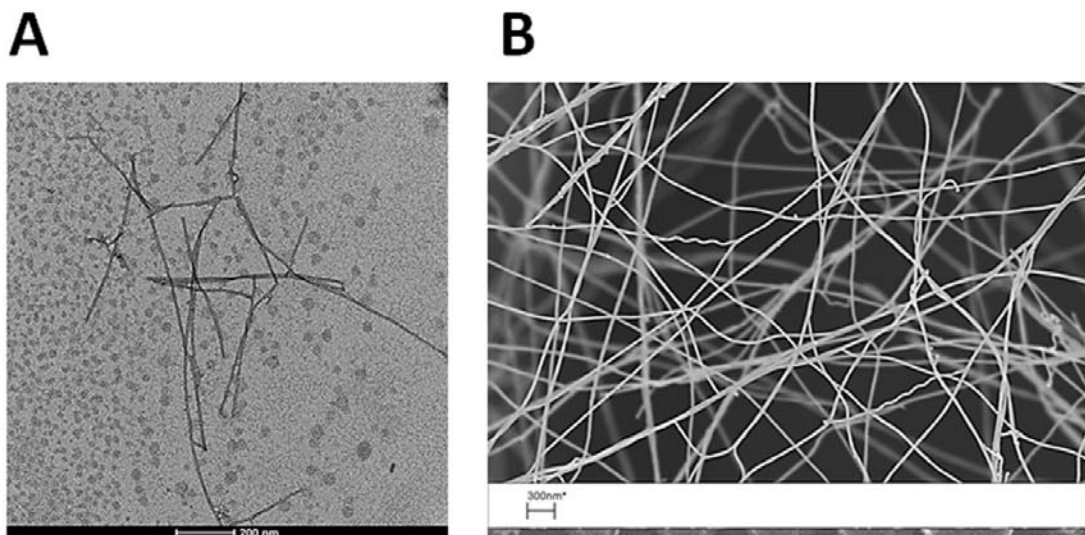


**Figure S14: SAXS scattering patterns of (A) monomers **D1** and **D2** cross-linked by the long crosslinker strand (**D1'**<sub>(12)</sub>**D2'**<sub>(12)</sub>), (B) **D1** and **D2** mixed without the crosslinker, (C) **D1** only, (D) **D2** only, and (E) backbone PA only. The complementary cross-linking strand (**D1'2'**) led to fiber bundling, as evidenced by the high slope in the low- $q$  region. In the absence of crosslinker, no bundles were observed.**

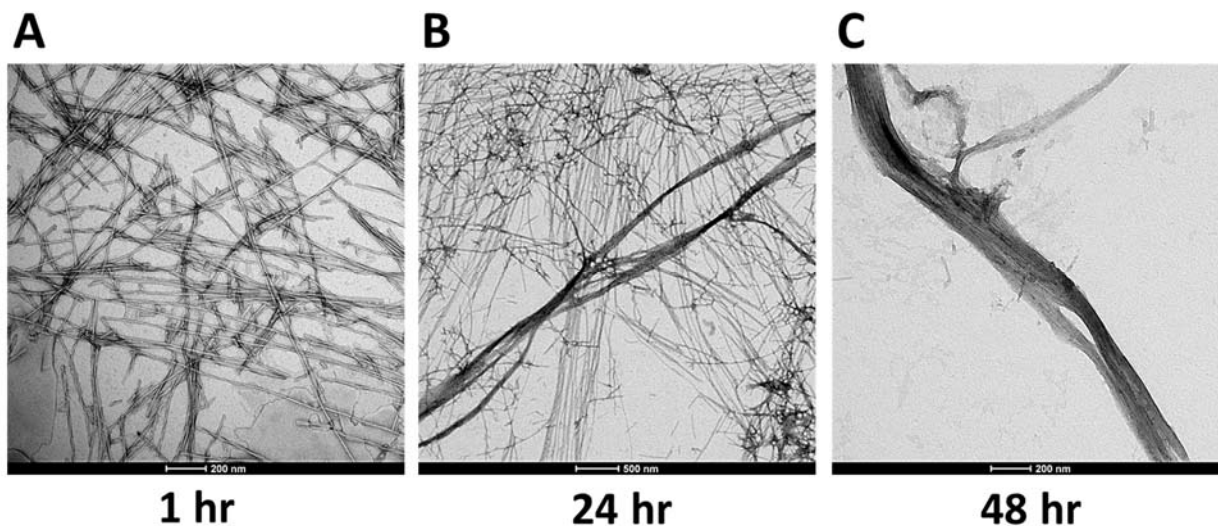




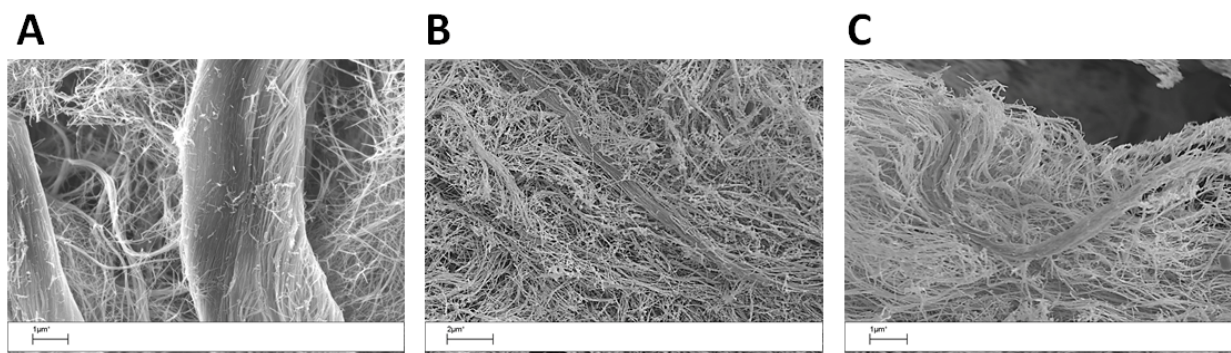
**Figure S15: Chemical structures and mass spectra of short tail weak  $\beta$ -sheet system.** Top – diluent PA, bottom – azido-PA used to link oligonucleotides via click chemistry.



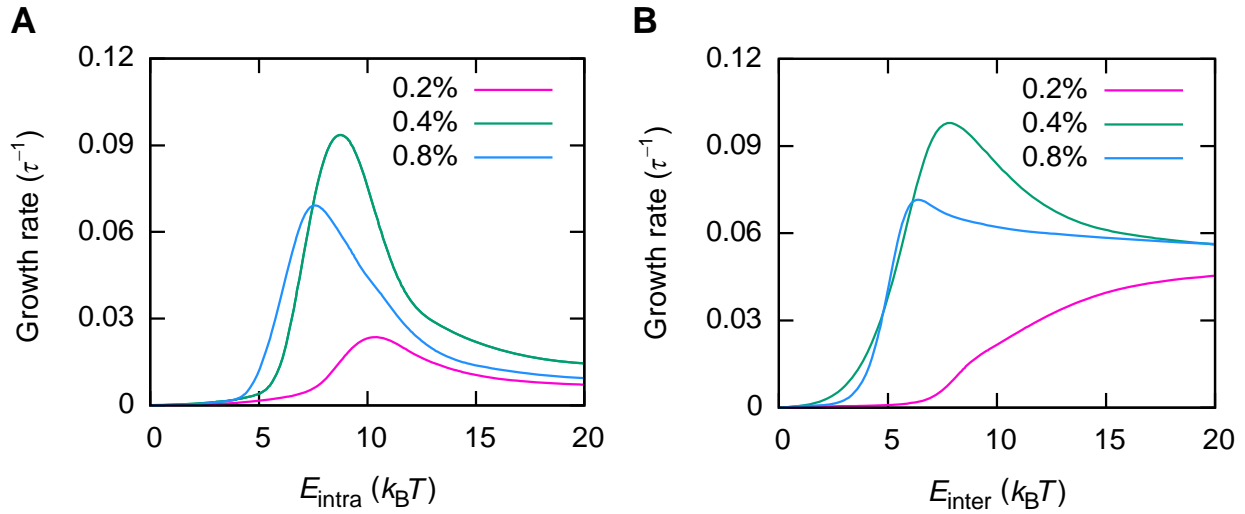
**Figure S16: Effect of hydrophobic tail and  $\beta$ -sheet on self-assembly of oligonucleotides-peptide amphiphiles:** (A) TEM of 1wt% C<sub>12</sub>G<sub>3</sub>A<sub>3</sub>E<sub>3</sub> PA showing a mixture of fibers and micelles. (B) SEM micrograph of 0.4 mole% co-assemblies of complementary monomers **short2** and **short2'**. Images show sparse fiber assembly and no bundled structures.



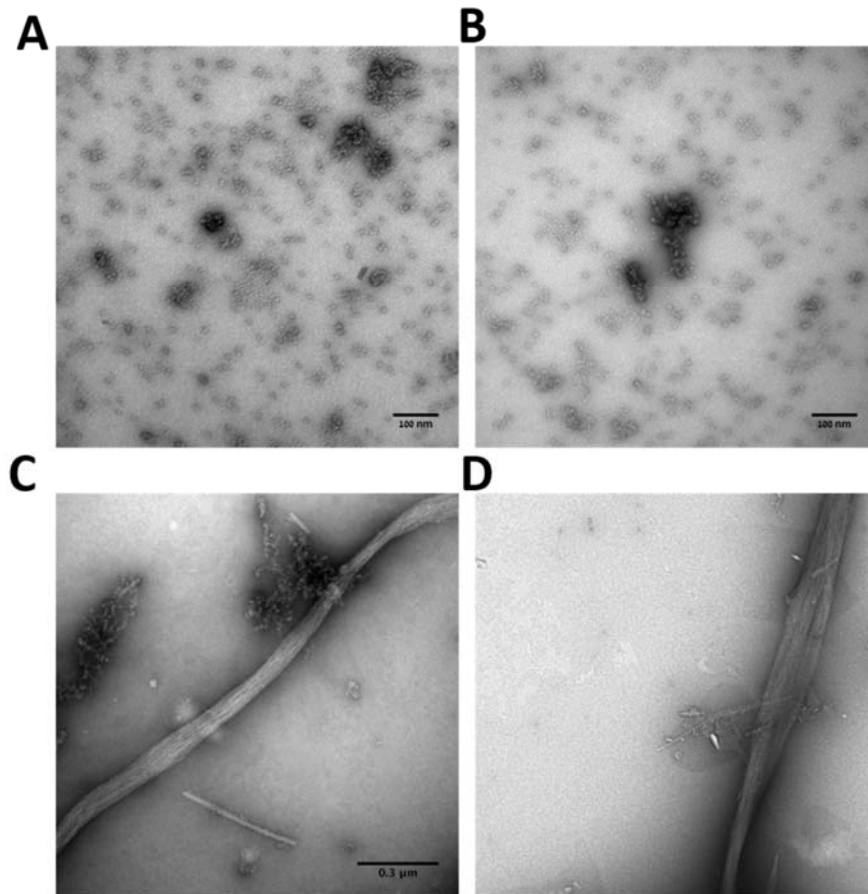
**Figure S17: Time-dependent bundle growth in the absence of salt:** TEM images after mixing complementary monomers **2** and **2'** in the absence of salt showing the time-dependent evolution of bundles over (A) 1 hour, (B) 1 day, and (C) 2 days.



**Figure S18: Effect of salt on bundle formation:** SEM micrographs after mixing and annealing complementary monomers **2** and **2'** in the presence of (A) 150 mM  $\text{Na}^+$  ions; (B) 150 mM  $\text{Na}^+$  and 10 mM  $\text{Ca}^{2+}$  ions; (C) 150 mM  $\text{Na}^+$  and 25 mM  $\text{Ca}^{2+}$  ions. Monovalent ions are sufficient to stabilize the formation of large bundles. The addition of divalent ions also induced electrostatic crosslinking on top of the DNA crosslinking, resulting in bundles as well as highly crosslinked DNA-depleted areas. The bundles formed in the presence of both monovalent and divalent ions appear to be smaller, probably due to fast electrostatic gelation that inhibits the redistribution of monomers.

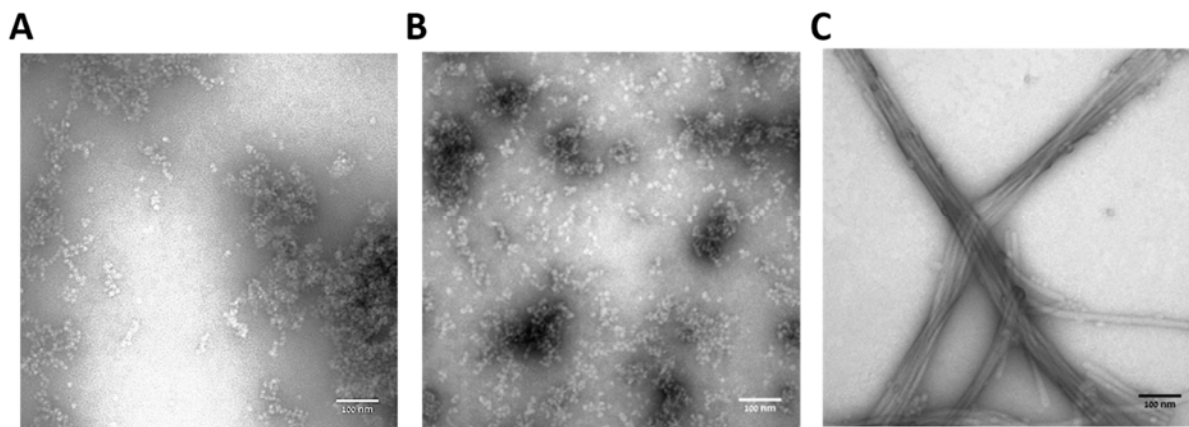


**Figure S19: Dependence of bundle growth on interaction energies at various DNA coverages.** (A) Fixed inter-fiber energy  $E_{\text{inter}} = 8 k_B T$ . As the intra-fiber energy  $E_{\text{intra}}$  was varied, the growth rate at intermediate DNA coverage (0.4%) was generally higher than in the other two cases. (B) Fixed intra-fiber energy  $E_{\text{intra}} = 8 k_B T$ . As the inter-fiber energy  $E_{\text{inter}}$  was varied, the intermediate DNA coverage (0.4%) again generally resulted in faster bundle growth than for 0.2% and 0.8%. This can be explained from the fact that too low DNA coverage suppresses large-scale DNA redistribution, whereas a too high DNA coverage causes kinetic “freezing” of the system.

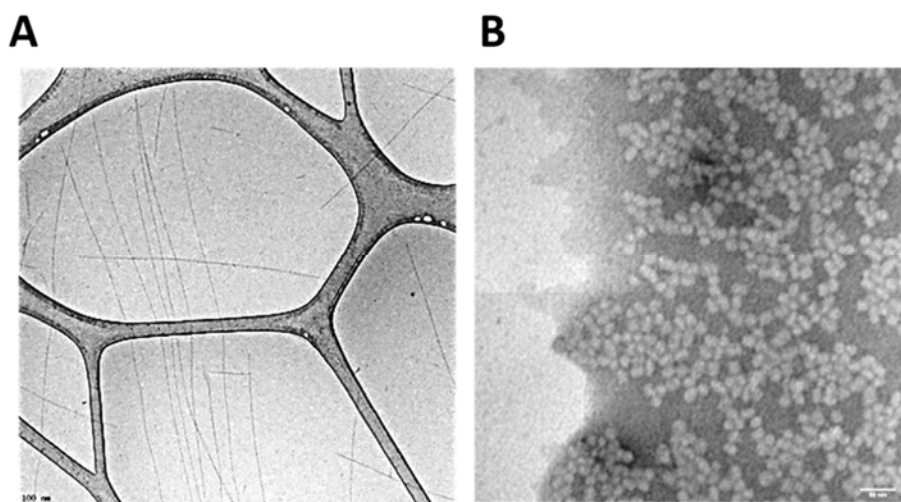


**Figure S20: TEM images of DNA monomers 2 and 2' in pure form. (A)** TEM images of the self-assembled structures formed by monomer 2; **(B)** by monomer 2'; **(C-D)** after mixing complementary monomers 2 and 2'.

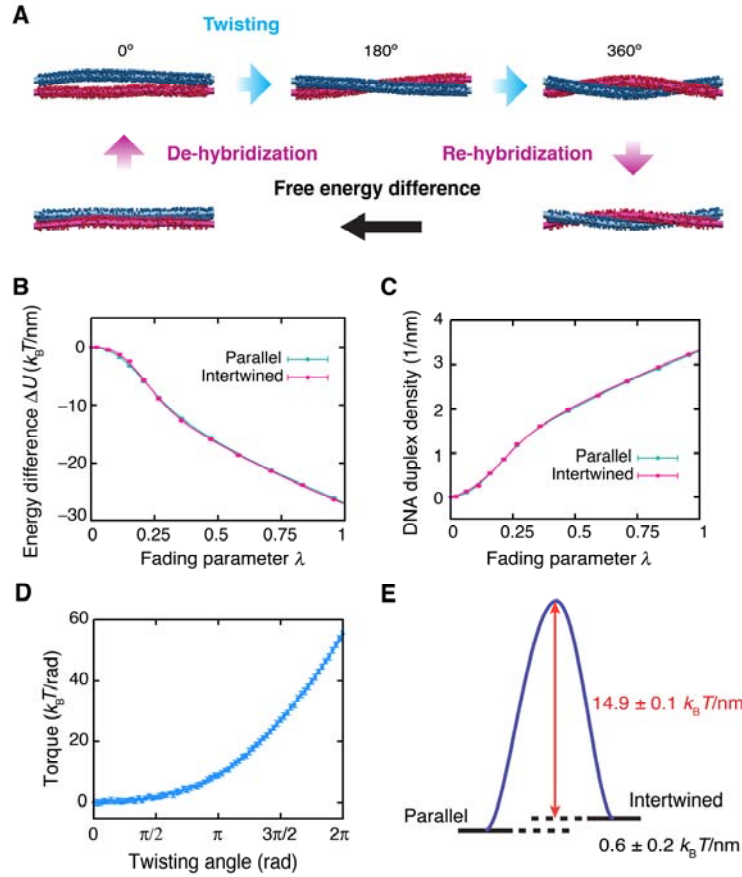




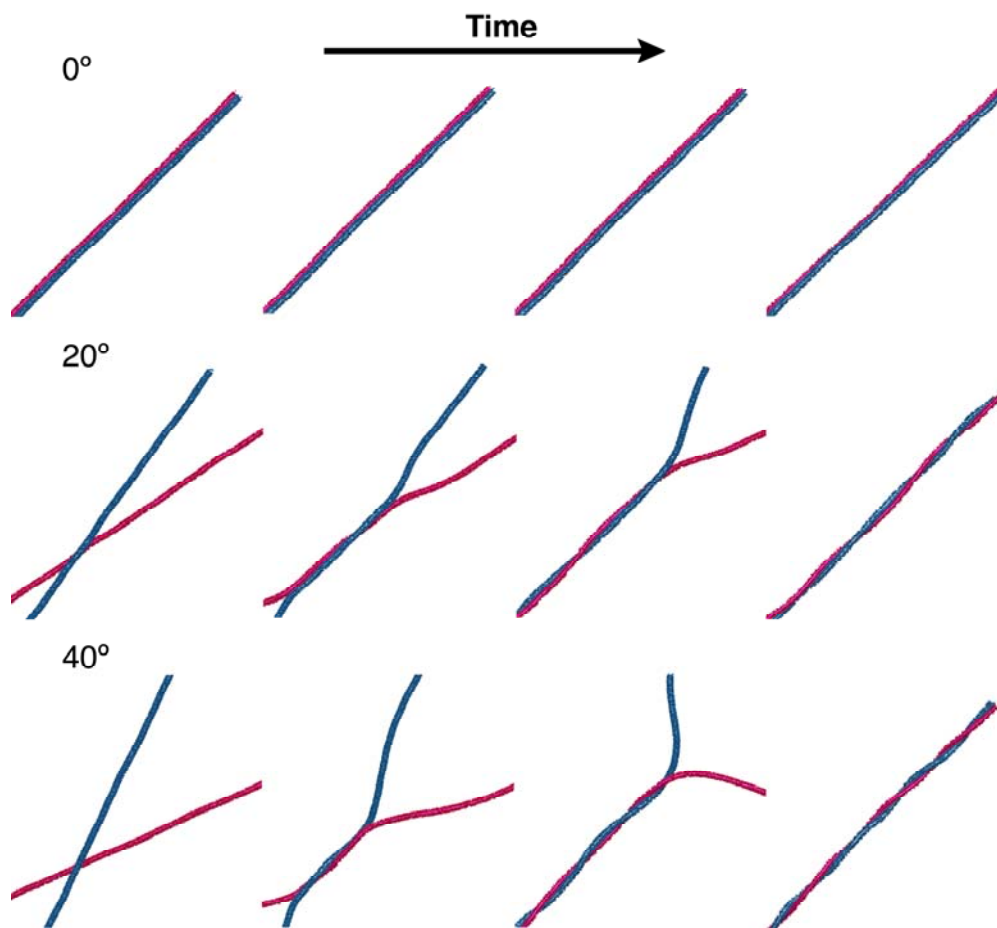
**Figure S21: TEM images of DNA monomers 3 and 3' in pure form. (A)** TEM images of the self-assembled structures formed by monomer **3**; **(B)** by monomer **3'**; **(C)** after mixing complementary monomers **3** and **3'**.



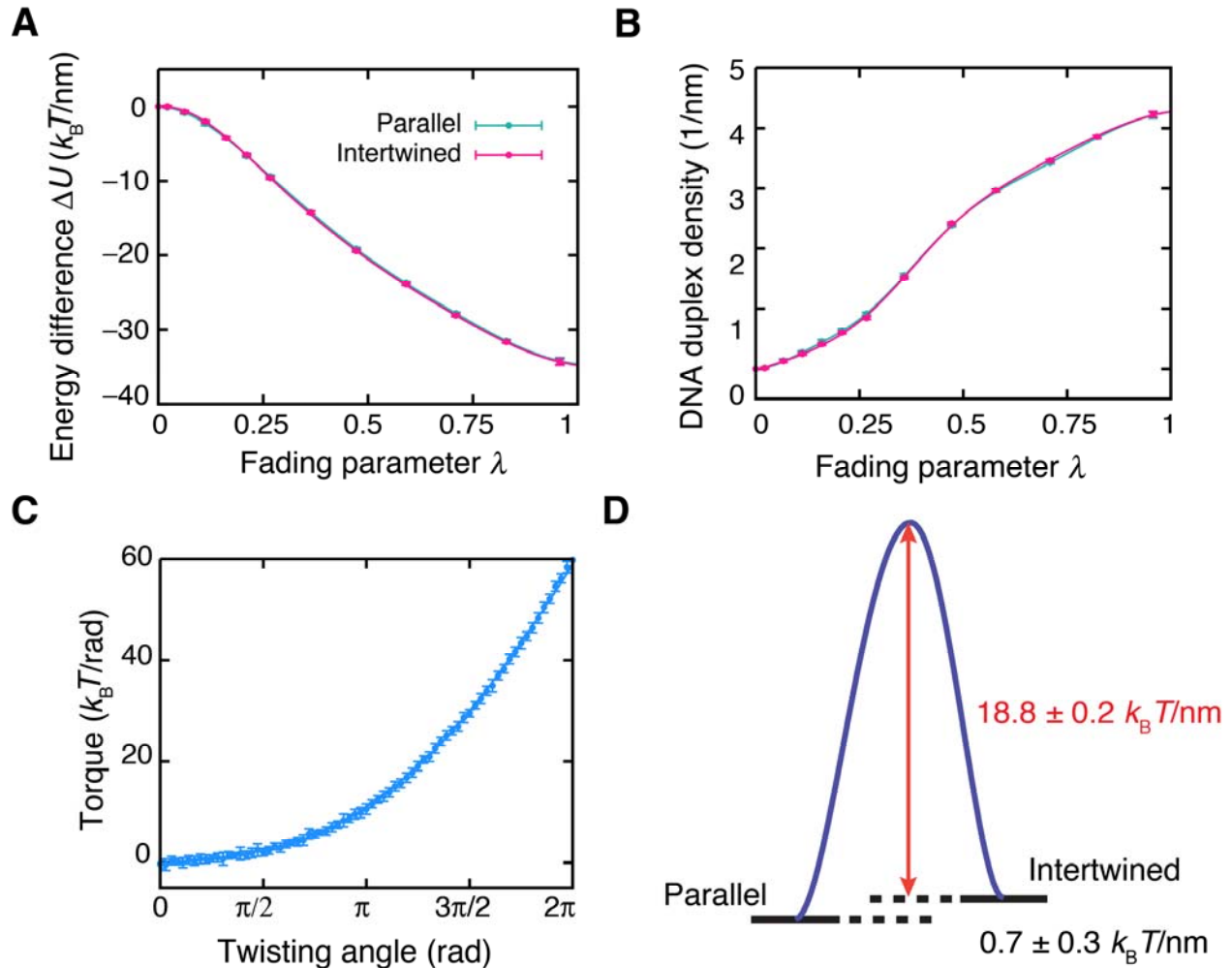
**Figure S22: TEM images of monomers 4 and 4' in pure form. (A)** Cryo-TEM images of the self-assembled structures formed by PNA-PA monomer **4** and **(B)** DNA-PA monomer **4'**.



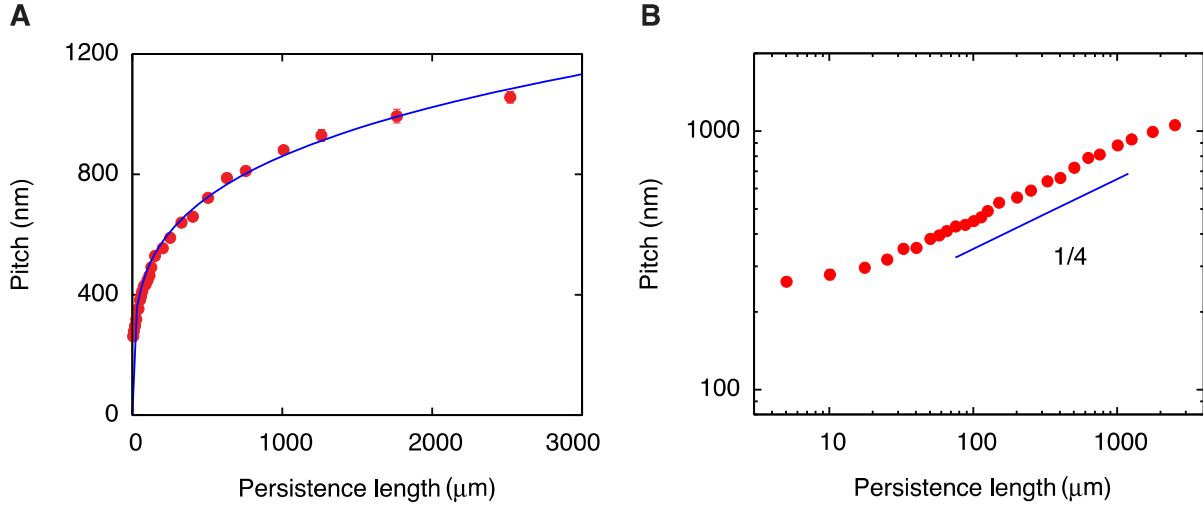
**Figure S23. Free-energy difference between the parallel and intertwined states of a complementary fiber pair.** (A) Pathway for thermodynamic integration. The free-energy change upon dehybridization in the parallel state and rehybridization of the intertwined state (purple arrows) was computed via Kirkwood integration. The free-energy change upon twisting was calculated by integrating the torque measured as a function of twist angle. We chose a 300 nm-long segment of two complementary PA fibers, so that a  $360^\circ$  twist generated the saturated intertwining pitch. (B) Average potential energy difference  $\Delta U$  between hybridized and dehybridized states as a function of Kirkwood parameter  $\lambda$ . For each reduced affinity  $\lambda$ , an ensemble of configurations was generated and  $\Delta U$  was computed as the difference between those configurations in their fully hybridized state and their unhybridized state. Results for both the parallel and the intertwined states are shown and were very similar. Integration of  $\Delta U$  over  $\lambda$  yielded the free-energy change due to hybridization as  $-15.0 \pm 0.1 k_B T/\text{nm}$  and  $-14.9 \pm 0.1 k_B T/\text{nm}$ , for a parallel and an intertwined pair, respectively. (C) Averaged density of DNA duplexes along the fibers. The extent of DNA hybridization was again very similar in both the parallel and the intertwined state. (D) Averaged torque as a function of twist angle. Integration of this torque yielded the free-energy cost of purely mechanical twisting in the absence of DNA hybridization as  $0.49 \pm 0.03 k_B T/\text{nm}$ . (E) Schematics of the free-energy comparison. The parallel state had a lower free energy than the intertwined state, albeit with a difference of only  $0.6 \pm 0.2 k_B T/\text{nm}$ . However, to switch between the two states, the fibers must first undergo dehybridization, which corresponds to a large barrier of  $14.9 \pm 0.1 k_B T/\text{nm}$ , which results in kinetic trapping of fibers that initially reside in the intertwined state.



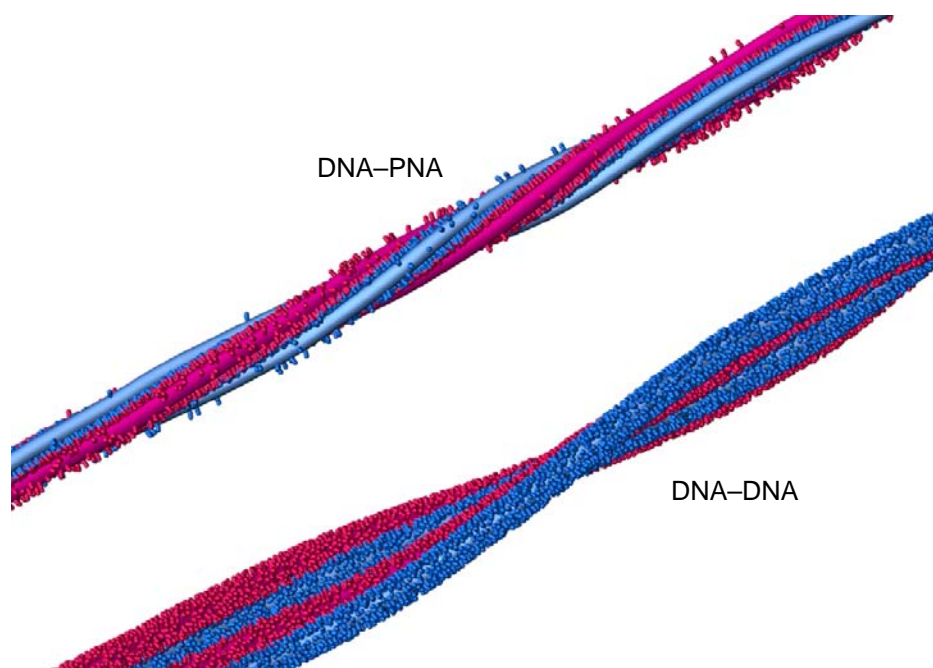
**Figure S24. Time evolution of two complementary fibers at different contact angles: 0° (top row), 20° (middle row), 40° (bottom row).** The fibers that were initially aligned in parallel did not show any tendency to intertwine, whereas fiber pairs that met at larger angles exhibited intertwining.



**Figure S25. Free-energy difference between the parallel and intertwined states for soft fibers.** To explore the effect of fiber deformability and a corresponding change in interaction surface on DNA hybridization between two fibers, we considered a modified fiber model. The excluded-volume interactions between the overlapping spheres that form the fiber backbone (Fig. S5) were reduced by a factor 10, allowing closer approach of two fibers, and the strengths of the backbone-DNA (B-D) and backbone-PNA (B-P) bonds were reduced by a factor 100 to  $k_{\text{bond}} = 10 k_B T/\sigma$ , allowing the side chains to be stretched and reach longer distances. The panels shown here are the counterparts of panels B-E in Fig. S22. **(A)** Average potential energy  $\Delta U$  between hybridized and dehybridized states as a function of Kirkwood parameter  $\lambda$ . The potential energy of hybridization is significantly larger than for the less deformable fibers in Fig. S22, yet remains very similar for parallel and intertwined pairs. **(B)** Averaged density of DNA duplexes along the fibers, which is correspondingly higher than for the less deformable fibers. **(C)** Averaged torque. As the softer fibers are wound more tightly, the torque is slightly higher than in Fig. S22. **(D)** Schematics of the free-energy comparison. Owing to the larger number of duplexes, the free-energy barrier between the intertwined and parallel states is higher than for the less deformable fibers. However, the free-energy difference between the two states is not affected by the softness, and the parallel state remains the thermodynamically favorable configuration.

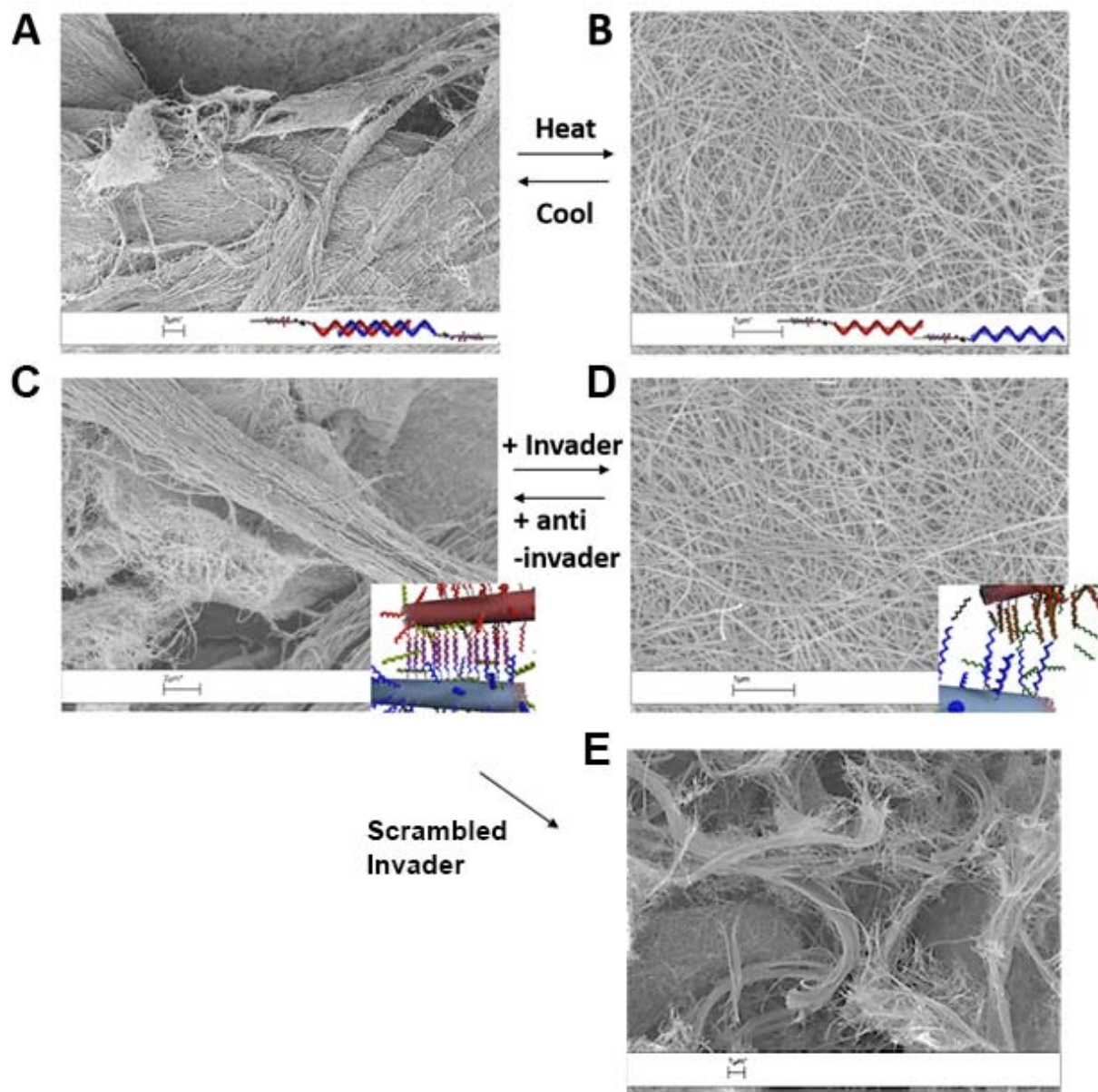


**Figure S26: Dependence of intertwining pitch on fiber stiffness.** (A) The intertwining pitch exhibited a power-law dependence on the persistence length of individual fibers, which can be described by an exponent  $1/4$ . (B) Same data on a logarithmic scale. This power-law dependence can be derived as follows. We parametrize a twisted fiber as  $(x, y, z) = (d \cos(\theta)/2, d \sin(\theta)/2, \theta p/(2\pi))$ , where  $d$  is the core-to-core distance between the two fibers (measured perpendicularly to the central axis of the twisted pair),  $p$  denotes the intertwining pitch, and  $\theta$  is the azimuthal angle. Then, the curvature generated by intertwining is  $\kappa = 2d/(d^2 + p^2/\pi^2)$ , which for  $p \gg d$  reduces to  $\kappa \approx 2\pi^2 d/p^2$ . The associated bending energy density follows as  $e = k_B T L_p \kappa^2/2 \approx 2\pi^2 k_B T L_p d^2/p^4$ , where  $L_p$  is the persistence length of a fiber. Assuming that intertwining occurs up to a bending energy penalty  $e_0$ , we find  $p = (2\pi^2 k_B T L_p d^2/e_0)^{1/4} \propto L_p^{1/4}$ , explaining the observed  $1/4$  power law.

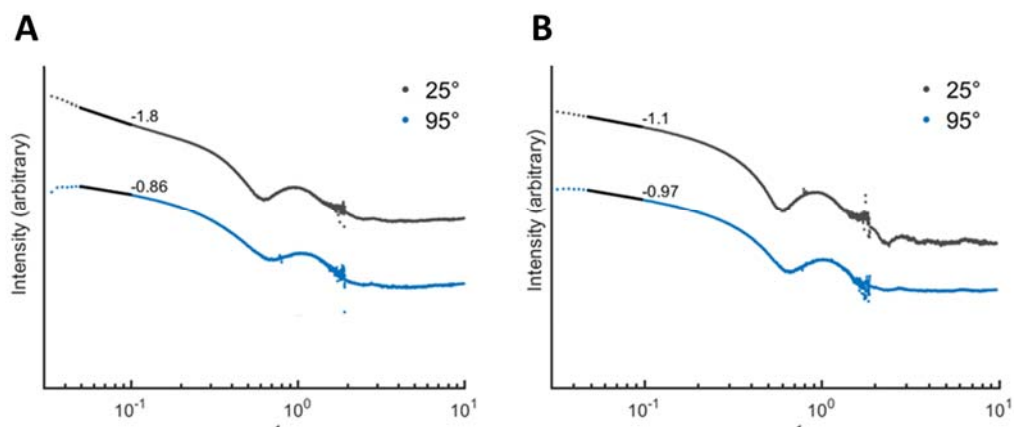


**Figure S27: Twisted bundles.** Compared to intertwining of two fibers, multiple-fiber twisting exhibited larger and less regular pitch. Moreover, due to the stronger electrostatic repulsion, the twisted bundle in the DNA-DNA system (bottom) developed into a ribbon-like structure, whereas a rod-like bundle was observed in the DNA-PNA system (top). Both systems had 40% nucleotide coverage.



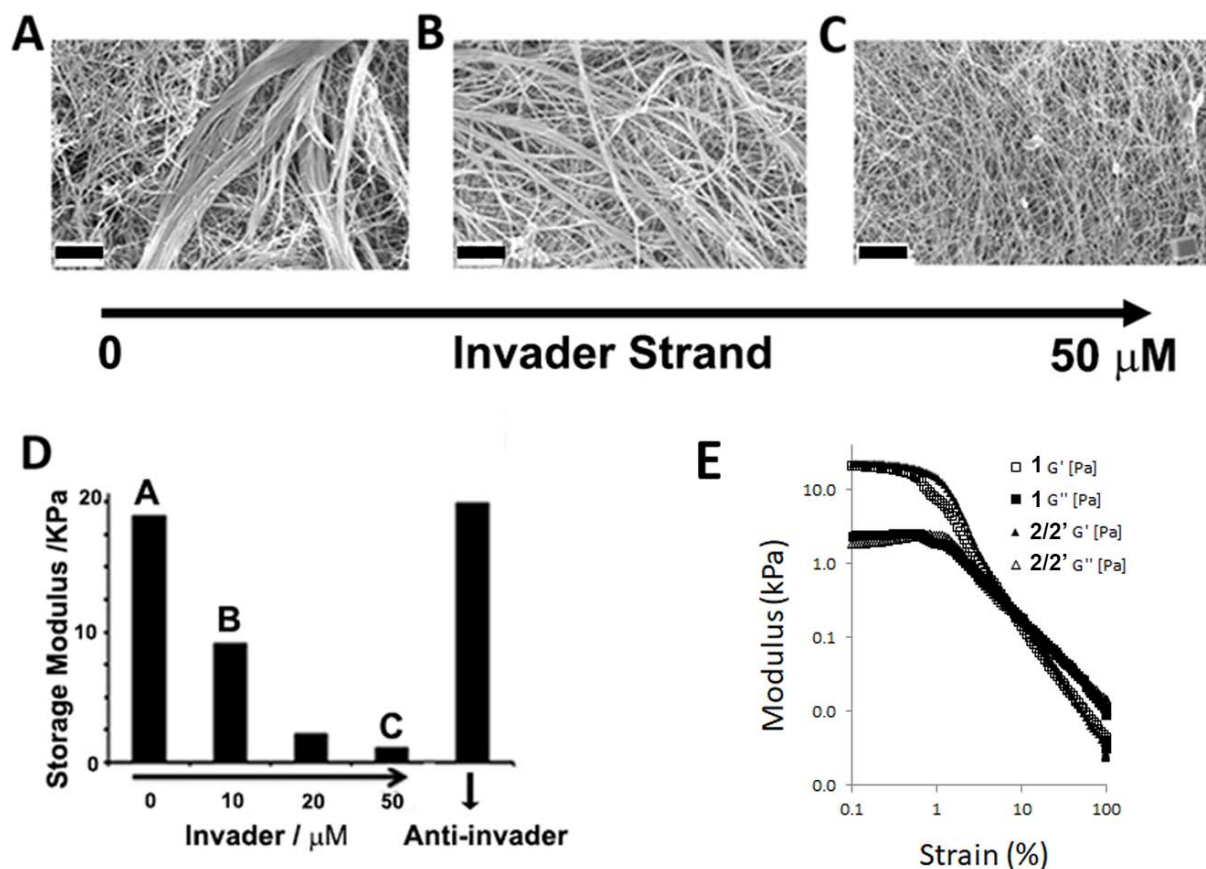


**Figure S28: SEM micrographs of reversible gelation.** (A-B) Thermal melting of the gel (95 °C over 30 min) resulted in individual fibers and subsequent cooling (over 60 min) causes the gel and bundles to reform. (C-D) Addition of the invader strand (for 30 min) resulted in individual fibers (right panel) and upon subsequent addition of the anti-invader (for 30 min) the gel and bundles reformed (left panel). (E) Addition of a scrambled invader strand (5'CAAAAGGTGGTAAACGTAATTAGGCCGACAGCCTTAATCGCAGATGAATGAGACGGAAC3') did not change the bundled structures (bottom panel), confirming that the hierarchical assembly is controlled by the specific DNA hybridization and that simply addition of a DNA strand does not result in morphological changes.

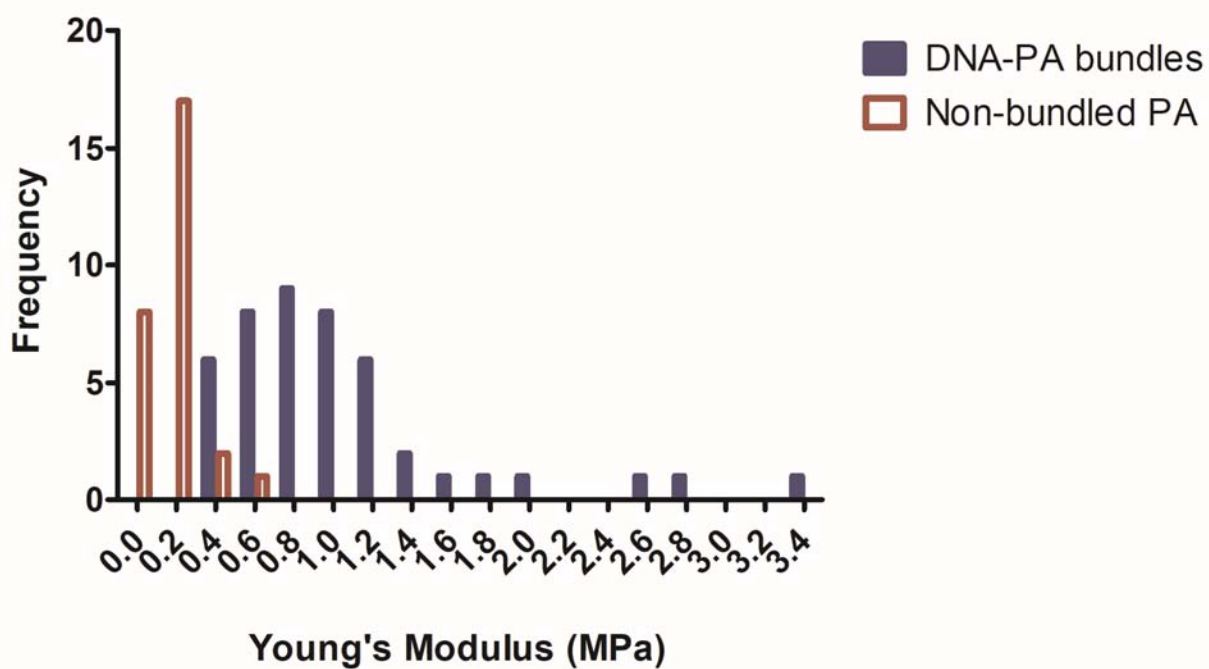


**Figure S29: SAXS scattering patterns at various temperatures of:** (A) Solutions containing monomers **2** and **2'**. (B) Solutions containing monomer **1**. The DNA-cross linked sample has a higher slope in the low- $q$  region indicating the formation of bundles. After heating, the slope decreases since the bundles are “melted” into individual fibers; the slope for the diluent PA (monomer **1**) is roughly unchanged indicating the existence of individual fibers in both conditions.

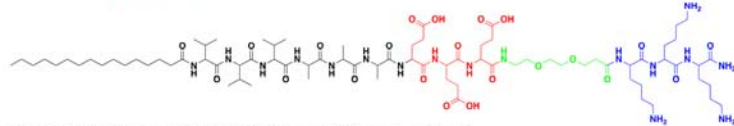




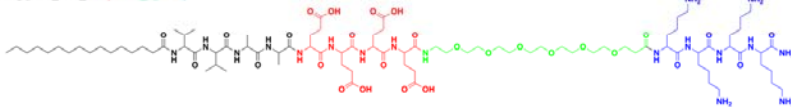
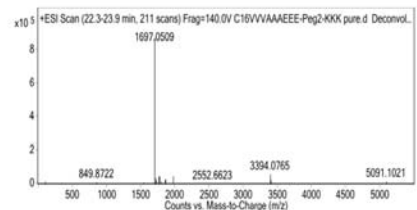
**Figure S30: Tunable bundle dimensions and mechanical properties.** (A-C) SEM micrographs showing bundle size in the presence of various concentrations of the invader strand: (A) no invader; (B) 10 mM; (C) 50 mM. Scale bar: 1 μm and relevant to all images. (D) Tunable reversible gelation: Storage modulus of DNA-crosslinked gels as a function of concentration of invader strand or anti-invader strand. (E) Storage modulus of a DNA-crosslinked gel and electrostatically crosslinked gel as a function of strain performed at 10 s<sup>-1</sup> frequency.



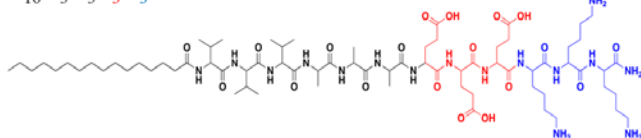
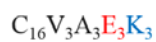
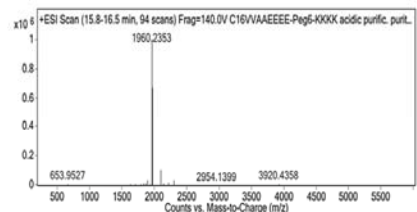
**Figure S31: Local stiffness of DNA-PA bundles:** Histogram of Young's Moduli for DNA-PA bundles ( $1.04 \pm 0.09$  MPa) and dispersed PA fibers ( $0.19 \pm 0.02$  MPa) measured using AFM nanoindentation;  $p < 0.0001$ , Mann-Whitney test.



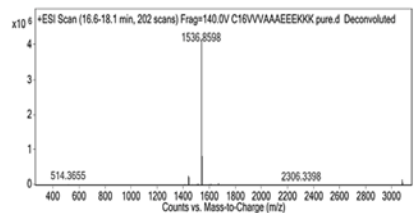
Expected Molecular Weight = 1697.14 g/mol



Expected Molecular Weight = 1960.43 g/mol

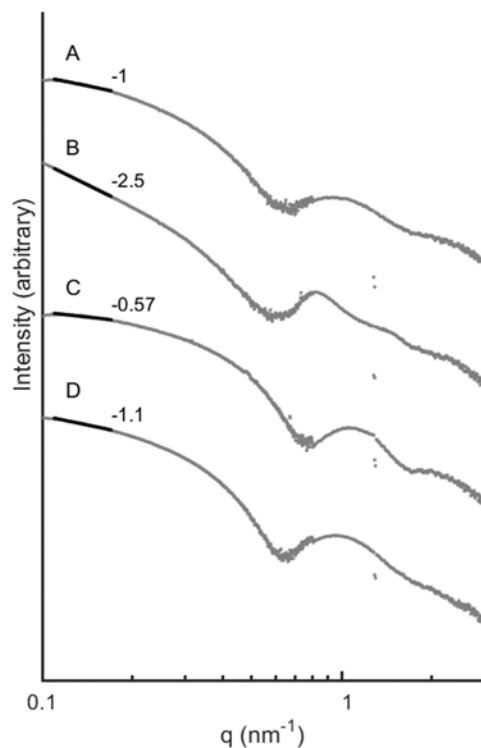


Expected Molecular Weight = 1537.95

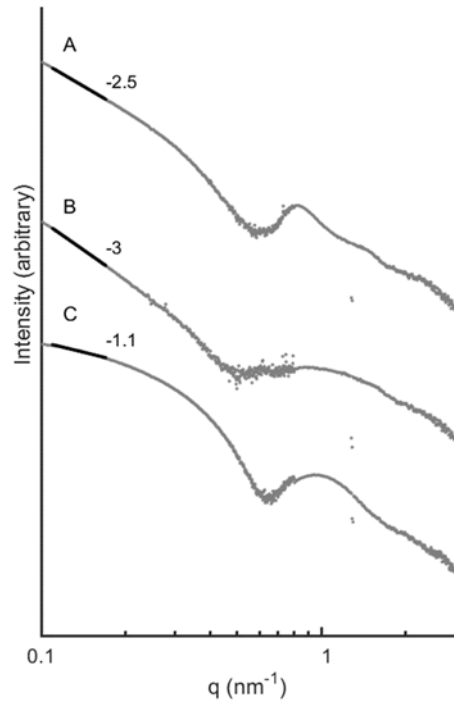


**Figure S32: Chemical structures and mass spectra of non-DNA system. Top – monomer (5), middle – monomer (6), bottom – monomer (7).**

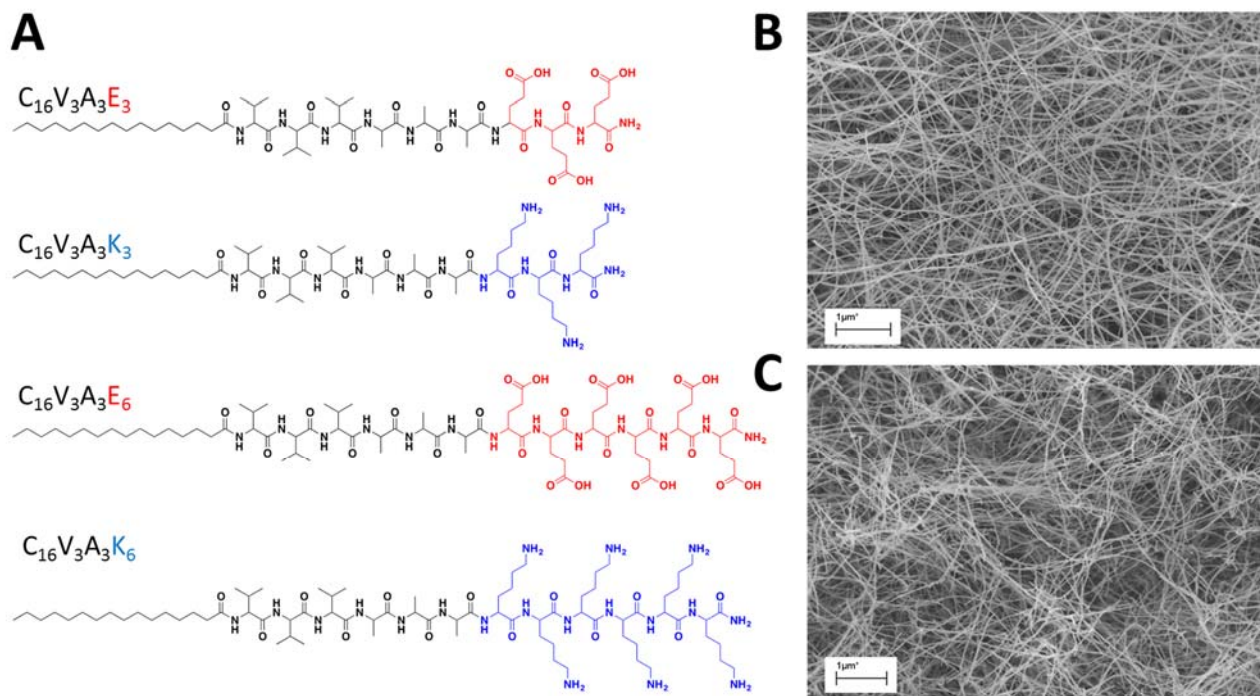




**Figure S34: SAXS scattering patterns of (A) Monomer 5 (E3-Peg2-K3-PA) annealed at pH 4, (B) pH 7, (C) pH 10, and (D) backbone PA only annealed at pH 7.** At pH 4 and 10, only basic or acidic residues respectively are charged so bundling does not occur, and the scattering pattern has a slope of  $-1$  in the low- $q$  region, indicating a cylindrical morphology. At pH 7, both acidic and basic residues are charged resulting in bundling due to electrostatic interactions and the scattering pattern has a slope of  $-2.5$  in the low- $q$  region, indicating larger structures.

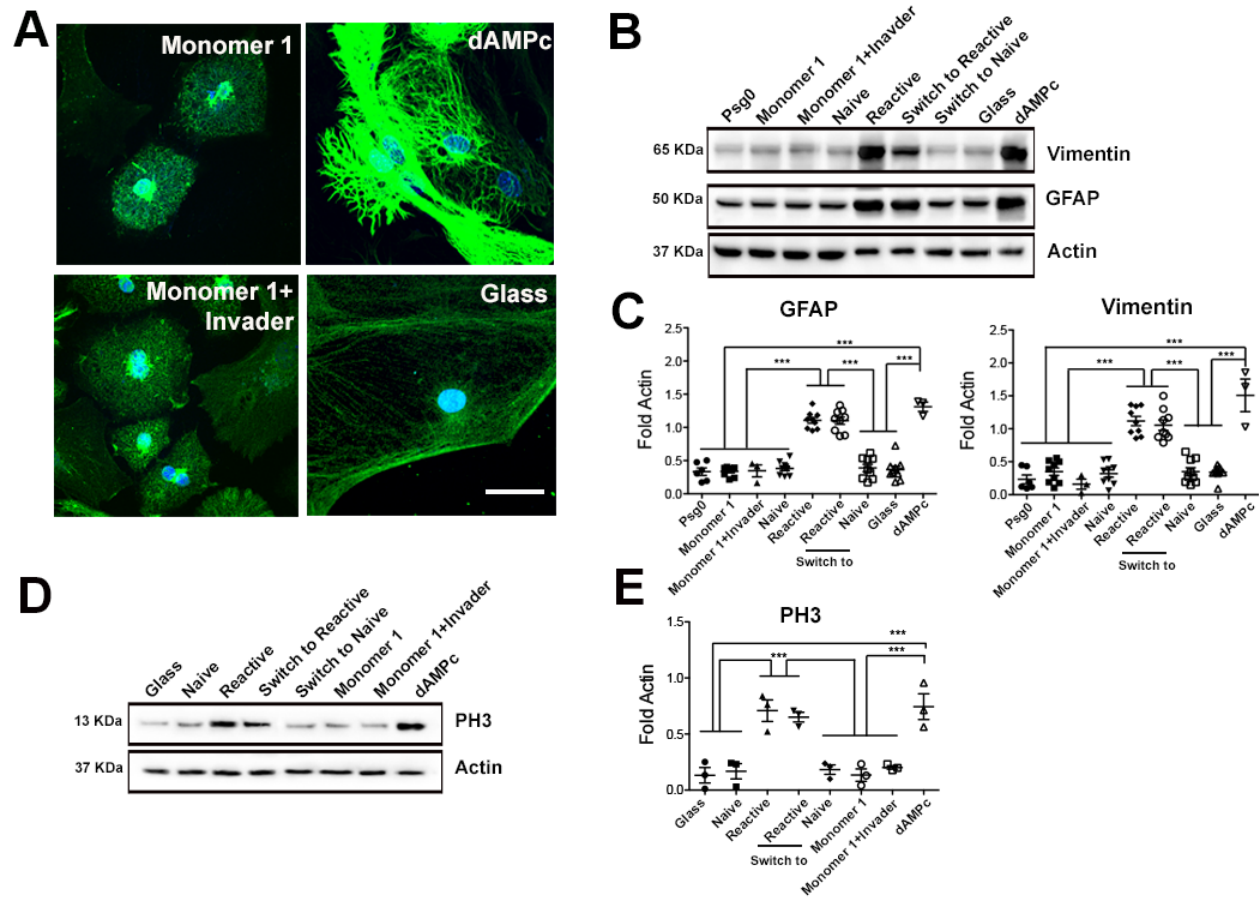


**Figure S35: SAXS scattering patterns of (A) Monomer 5 (E3-Peg2-K3-PA) annealed at pH 7, (B) Monomer 6 (E4-Peg6-K4-PA) annealed at pH 7, and (C) Backbone PA annealed at pH 7. PAs with complementary charged regions bundled to form large aggregates, indicated by a steep negative slope in the low- $q$  region.**



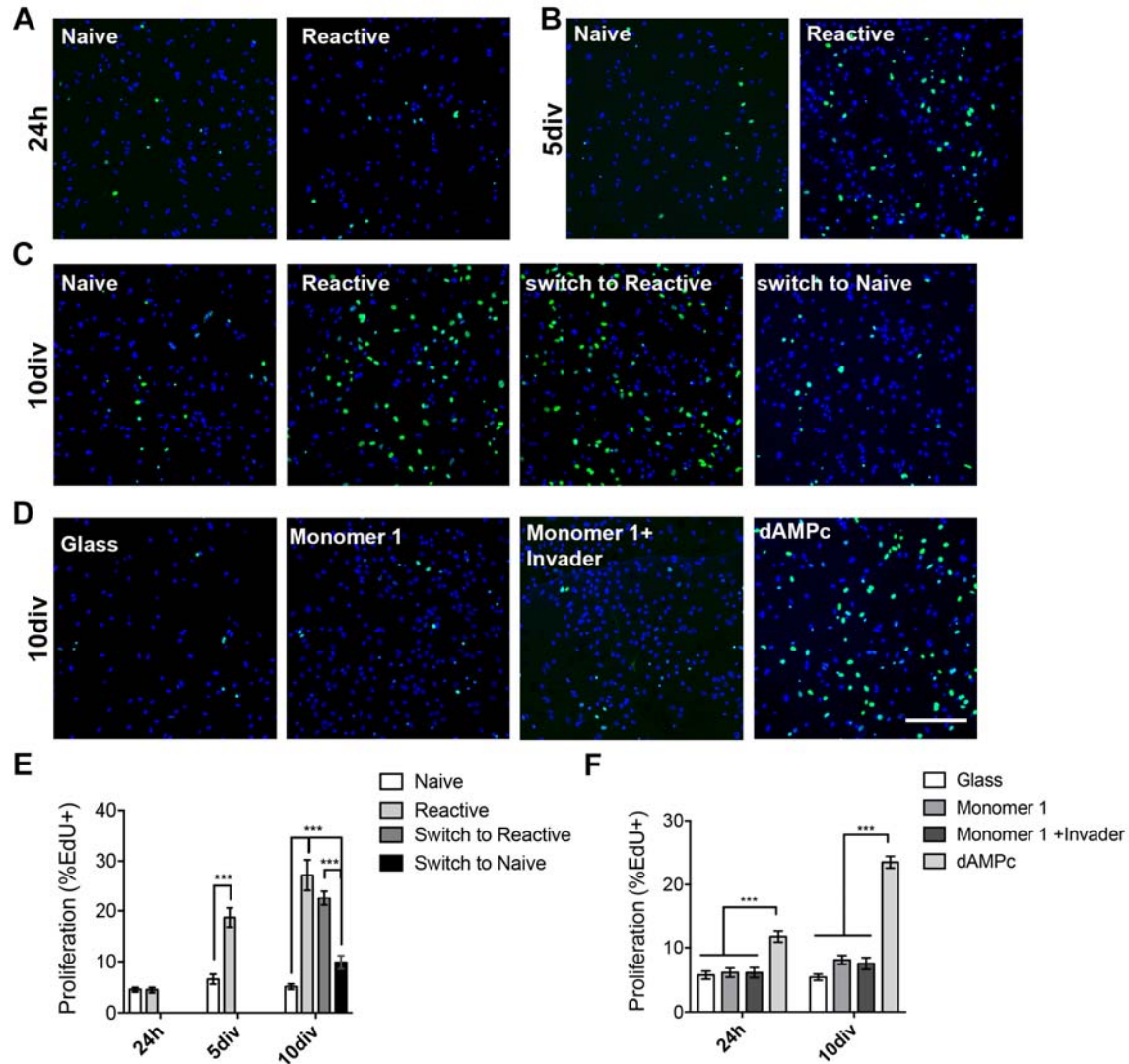
**Figure S36: Mixing oppositely charged fibers** (A) Chemical structures of peptide amphiphiles with a charged domain of three or six amino acids. (B-C) SEM micrographs of the hydrogels formed upon mixing oppositely charged fibers with three charged amino acids, (B) or six charged amino acids, (C).



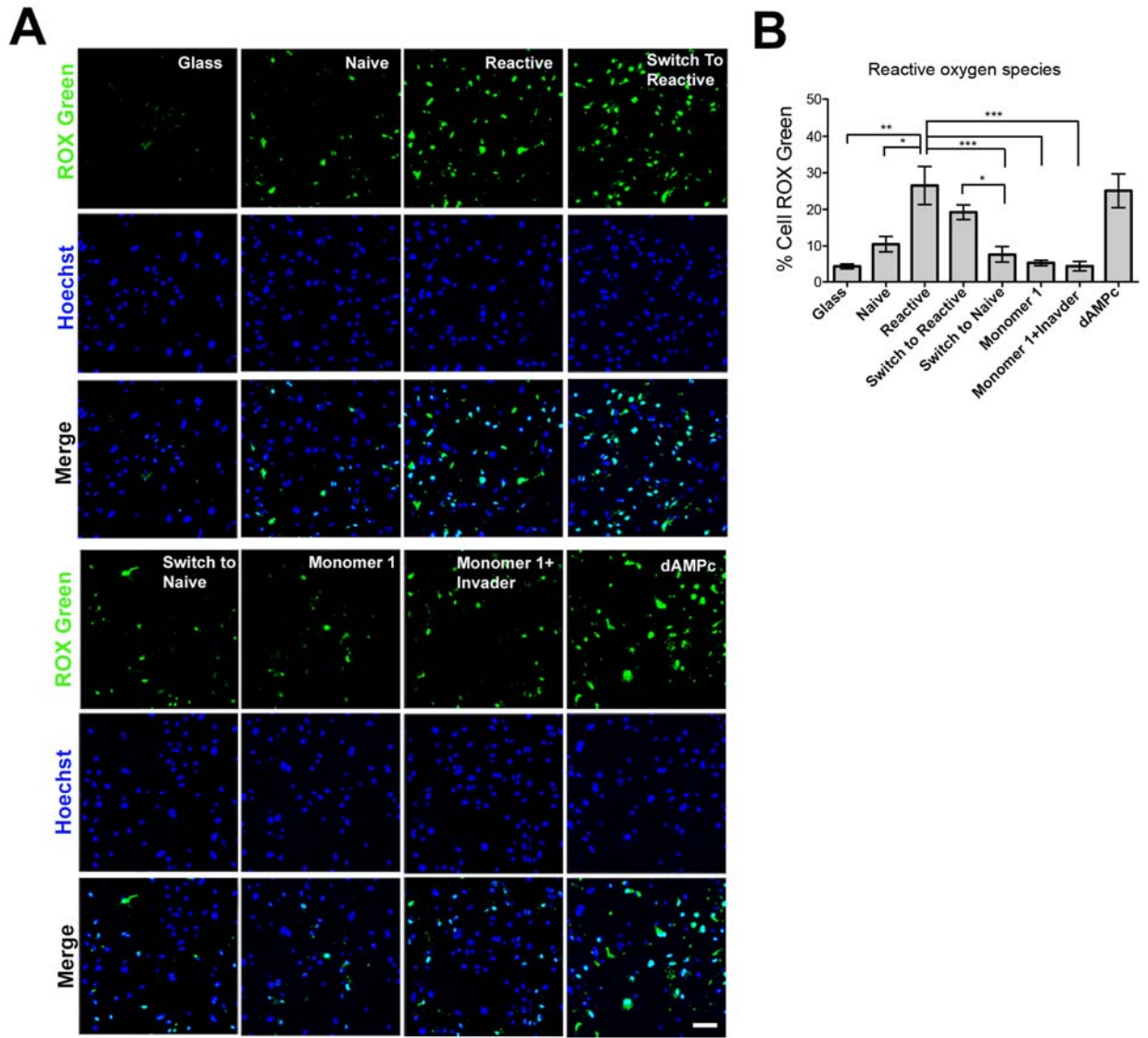


**Figure S37: Dynamic modulation of astroglial phenotype.** (A) Confocal images of astroglial cells plated on non-DNA containing hydrogels (Monomer 1), on monomer 1 hydrogels after addition of Invader strand, in the presence of dibutyryl cyclic adenosine monophosphate (dAMPc) and on Glass (control condition). Staining for GFAP (mature/reactive glial marker, green), and DAPI (nuclei, blue). (B) Western blot analysis of GFAP and Vimentin (mature/reactive glial markers) in astroglial cells measured after 10 days *in vitro* on individual fibers (Naive), on bundled fibers (Reactive), after switching from individual fibers to bundles (Switch to Reactive) and from bundles to individual fibers (Switch to Naive), on non-DNA containing hydrogels (Monomer 1), monomer 1 hydrogels after addition of Invader strand (Monomer 1+Invader), in the presence of dibutyryl cyclic adenosine monophosphate (dAMPc) and on Glass (control condition). Psg0 corresponds to first passage of astrocytes before culture them on the experimental conditions. (C) Relative expression of proteins derived from western blots in (B). (D) Western blot analysis of PH3 (proliferation marker) in astroglial cells measured after 10 days *in vitro* on the indicated substrates. (E) Relative expression of PH3 derived from western blots in (D). All values were normalized to Actin expression. (\*  $p < 0.05$ ; \*\*  $p < 0.01$ ; \*\*\*\*  $p < 0.0001$ , LSD test). Scale bar: 20  $\mu\text{m}$  and relevant to all images.

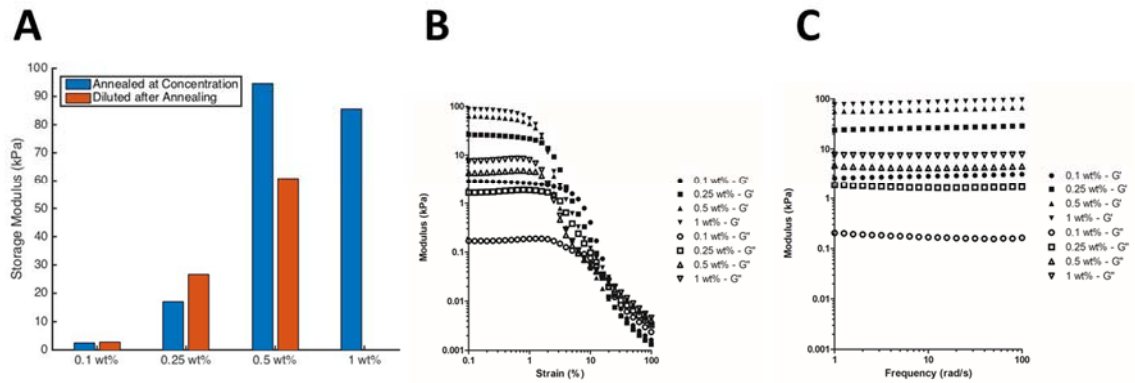




**Figure S38: Proliferation assay in astroglial cells.** (A-C) Immunofluorescent images of astroglial cells stained with EdU (proliferative cells, green) and DAPI (Nuclei, blue) on individual fibers (Naive) and bundled fibers (Reactive) for (A) 24h, (B) 5 days *in vitro* (div) and (C) 10 div after switching from individual fibers to bundles (Switch to Reactive) and from bundles to individual fibers (Switch to Naive). (D) Immunofluorescence images of astroglial cells stained with EdU (proliferative cells, green) and DAPI (Nuclei, blue) control condition (Glass), non-DNA containing hydrogels (Monomer 1), after addition of Invader strand to monomer 1 hydrogels (Monomer 1+Invader) and in the presence of dibutyryl cyclic adenosine monophosphate (dAMPc). (E, F) Quantification of the percentage of cells that have incorporated EdU (24h incubation) in the different conditions mentioned in (A-D). (\*\*\*)  $p < 0.001$ , LSD test). Scale bar: 100  $\mu\text{m}$  and relevant to all images.



**Figure S39: Reactive oxygen species in astroglial cell.** (A) Immunofluorescence images of astroglial cells stained with ROX Green (reactive oxygen species, green) and Hoechst (Nuclei, blue) on control condition (Glass), individual fibers (Naive), bundled fibers (Reactive), after switching from individual fibers to bundles (Switch to Reactive) and from bundles to individual fibers (Switch to Naive), on non-DNA containing hydrogels (Monomer 1), after addition of Invader strand to monomer 1 hydrogels (Monomer 1+Invader) and in the presence of dibutylryl cyclic adenosine monophosphate (dAMPc). (B) Reactive oxygen species (ROS) quantification versus total number of cells (Hoechst) in the different conditions mentioned in (A). (\*  $p < 0.05$ , \*\*  $p < 0.01$ , \*\*\*  $p < 0.001$ , LSD test). Scale bar: 100  $\mu\text{m}$  and relevant to all images.






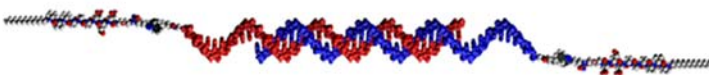




**Figure S40: Mechanical properties of calcium-gelled monomer 1.** Storage modulus of DNA-free gels made from the E3 PA fibers and added calcium. Samples were measured either by annealing the PA at the tested concentration (blue), or by diluting the PA from samples annealed at 1 wt% prior to testing (orange). Gels annealed at 0.25 wt% have similar mechanical properties to the DNA-crosslinked gels. **(B-C)** Storage modulus of E3 gels at various concentrations as a function of **(B)** strain and **(C)** frequency. Frequency sweeps were performed at 0.1 % strain and strain sweeps were performed at  $10 \text{ s}^{-1}$  frequency.

## Tables:

Molecule Name and Number	PA Sequence / DNA Sequence (5' to 3')
monomer 1	C <sub>16</sub> V <sub>3</sub> A <sub>3</sub> E <sub>3</sub>
monomer 2	C <sub>16</sub> V <sub>3</sub> A <sub>3</sub> E <sub>3</sub> (Peg) <sub>10</sub> CCTCCTGTTATGATCGTTATATTTTATTATTCCACTGCCGCGTCA-3'
monomer 2'	C <sub>16</sub> V <sub>3</sub> A <sub>3</sub> E <sub>3</sub> (Peg) <sub>10</sub> AGGTCGTGACAAGAATGACGCGGCAGTGGAATAATAAAATATAAC-3'
monomer 3	C <sub>16</sub> V <sub>3</sub> A <sub>3</sub> E <sub>3</sub> (Peg) <sub>10</sub> CTCAGTGGACAGCC
monomer 3'	C <sub>16</sub> V <sub>3</sub> A <sub>3</sub> E <sub>3</sub> (Peg) <sub>10</sub> GGCTGTCCACTGAG
monomer 4	C <sub>16</sub> V <sub>3</sub> A <sub>3</sub> E <sub>3</sub> (PEG) <sub>2</sub> CTGTGCGTAC
monomer 4'	C <sub>16</sub> V <sub>3</sub> A <sub>3</sub> E <sub>3</sub> (PEG) <sub>2</sub> TTGTACGCACAG
Invader	CTCAGTGGACAGCCTGACGCGGCAGTGGAATAATAAAATATAACGATCATAACAGGAGG
Anti-invader	CCTCCTGTTATGATCGTTATATTTTATTATTCCACTGCCGCGTCAGGCTGTCCACTGAG
monomer 5	C <sub>16</sub> V <sub>3</sub> A <sub>3</sub> E <sub>3</sub> Peg <sub>2</sub> K <sub>3</sub>
monomer 6	C <sub>16</sub> V <sub>2</sub> A <sub>2</sub> E <sub>4</sub> Peg <sub>6</sub> K <sub>4</sub>
monomer 7	C <sub>16</sub> V <sub>3</sub> A <sub>3</sub> E <sub>3</sub> K <sub>3</sub>

**Table S1: Names and corresponding sequences of all monomers used in this manuscript.**

Complementary domains of the different pairs are shown in green. **2/2'** pair (30 bp; GC content 36.7%; T<sub>m</sub> 63.1 °C); **3/3'** pair (14 bp; GC content 64.3%; T<sub>m</sub> 55.3 °C). **4/4'** PNA/DNA pair (10 bp; GC content 60%; T<sub>m</sub> 55.7 °C).

Monomer 1	
Monomer 2	
Monomer 2'	
2 / 2'	
Invader Strand	
2 / Invader	
Anti-invader Strand	
Invader / Anti-invader	

**Table S2: Names and corresponding molecular graphics illustrations of DNA monomers and their interactions.**

Bead pair	$k_{\text{bond}}$	$r_0$
B-B	$10^4 k_B T / \sigma_c^2$	$0.1 \sigma_c$
B-D or B-P	$10^4 k_B T / \sigma_c^2$	$0.6 \sigma_c$
D-D or P-P	$10^4 k_B T / \sigma_c^2$	$0.135 \sigma_c$
Hybridized D-P	$1.4 \times 10^3 k_B T / \sigma_c^2$	$0.16 \sigma_c$

**Table S3: Parameters for the harmonic bond potentials.** The first column specifies the bead pairs: backbone (B), DNA (D), and PNA (P).

Bead triplet	$k_{\text{angle}}$	$\theta$
BBB	$10^4 k_B T / \text{rad}^2$	$180^\circ$
BBD (or BBP)	$10^4 k_B T / \text{rad}^2$	$90^\circ$
BDD (or BPP)	$k_B T / \text{rad}^2$	$180^\circ$
DDD (or PPP)	$0.3 k_B T / \text{rad}^2$	$180^\circ$
DDD (or PPP) after hybridization	$7.5 k_B T / \text{rad}^2$	$180^\circ$

**Table S4: Parameters for the harmonic angle potentials.** Different 3-bead sequences of backbone (B), DNA (D), and PNA (P) are shown.

**Movie S1. Intertwining of two complementary fibers.** The two fibers were 3  $\mu\text{m}$  long, grafted with 10-base-long DNA (red) and complementary PNA (blue), respectively. Prior to intertwining, the two fibers met at an initial contact angle of  $20^\circ$ .



## References

1. G. M. Whitesides, B. Grzybowski, Self-assembly at all scales. *Science* **295**, 2418–2421 (2002). [doi:10.1126/science.1070821](https://doi.org/10.1126/science.1070821) [Medline](#)
2. S. Zhang, Fabrication of novel biomaterials through molecular self-assembly. *Nat. Biotechnol.* **21**, 1171–1178 (2003). [doi:10.1038/nbt874](https://doi.org/10.1038/nbt874) [Medline](#)
3. D. Needleman, Z. Dogic, Active matter at the interface between materials science and cell biology. *Nat. Rev. Mater.* **2**, 17048 (2017). [doi:10.1038/natrevmats.2017.48](https://doi.org/10.1038/natrevmats.2017.48)
4. A. J. Ridley, A. Hall, The small GTP-binding protein rho regulates the assembly of focal adhesions and actin stress fibers in response to growth factors. *Cell* **70**, 389–399 (1992). [doi:10.1016/0092-8674\(92\)90163-7](https://doi.org/10.1016/0092-8674(92)90163-7) [Medline](#)
5. C. G. dos Remedios, D. Chhabra, M. Kekic, I. V. Dedova, M. Tsubakihara, D. A. Berry, N. J. Nosworthy, Actin binding proteins: Regulation of cytoskeletal microfilaments. *Physiol. Rev.* **83**, 433–473 (2003). [doi:10.1152/physrev.00026.2002](https://doi.org/10.1152/physrev.00026.2002) [Medline](#)
6. H. Qiu, Z. M. Hudson, M. A. Winnik, I. Manners, Multidimensional hierarchical self-assembly of amphiphilic cylindrical block comicelles. *Science* **347**, 1329–1332 (2015). [doi:10.1126/science.1261816](https://doi.org/10.1126/science.1261816) [Medline](#)
7. R. M. Capito, H. S. Azevedo, Y. S. Velichko, A. Mata, S. I. Stupp, Self-assembly of large and small molecules into hierarchically ordered sacs and membranes. *Science* **319**, 1812–1816 (2008). [doi:10.1126/science.1154586](https://doi.org/10.1126/science.1154586) [Medline](#)
8. A. Aggeli, I. A. Nyrkova, M. Bell, R. Harding, L. Carrick, T. C. B. McLeish, A. N. Semenov, N. Boden, Hierarchical self-assembly of chiral rod-like molecules as a model for peptide  $\beta$ -sheet tapes, ribbons, fibrils, and fibers. *Proc. Natl. Acad. Sci. U.S.A.* **98**, 11857–11862 (2001). [doi:10.1073/pnas.191250198](https://doi.org/10.1073/pnas.191250198) [Medline](#)
9. S. Zhang, M. A. Greenfield, A. Mata, L. C. Palmer, R. Bitton, J. R. Mantei, C. Aparicio, M. O. de la Cruz, S. I. Stupp, A self-assembly pathway to aligned monodomain gels. *Nat. Mater.* **9**, 594–601 (2010). [doi:10.1038/nmat2778](https://doi.org/10.1038/nmat2778) [Medline](#)
10. M. Kumar, N. L. Ing, V. Narang, N. K. Wijerathne, A. I. Hochbaum, R. V. Ulijn, Amino-acid-encoded biocatalytic self-assembly enables the formation of transient conducting nanostructures. *Nat. Chem.* **10**, 696–703 (2018). [doi:10.1038/s41557-018-0047-2](https://doi.org/10.1038/s41557-018-0047-2) [Medline](#)
11. L. E. O’Leary, J. A. Fallas, E. L. Bakota, M. K. Kang, J. D. Hartgerink, Multi-hierarchical self-assembly of a collagen mimetic peptide from triple helix to nanofibre and hydrogel. *Nat. Chem.* **3**, 821–828 (2011). [doi:10.1038/nchem.1123](https://doi.org/10.1038/nchem.1123) [Medline](#)
12. Y. Kim, R. J. Macfarlane, M. R. Jones, C. A. Mirkin, Transmutable nanoparticles with reconfigurable surface ligands. *Science* **351**, 579–582 (2016). [doi:10.1126/science.aad2212](https://doi.org/10.1126/science.aad2212) [Medline](#)

13. G. Seelig, D. Soloveichik, D. Y. Zhang, E. Winfree, Enzyme-free nucleic acid logic circuits. *Science* **314**, 1585–1588 (2006). [doi:10.1126/science.1132493](https://doi.org/10.1126/science.1132493) [Medline](#)
14. R. M. da Silva, D. van der Zwaag, L. Albertazzi, S. S. Lee, E. W. Meijer, S. I. Stupp, Super-resolution microscopy reveals structural diversity in molecular exchange among peptide amphiphile nanofibres. *Nat. Commun.* **7**, 11561 (2016). [doi:10.1038/ncomms11561](https://doi.org/10.1038/ncomms11561) [Medline](#)
15. W. P. Daley, S. B. Peters, M. Larsen, Extracellular matrix dynamics in development and regenerative medicine. *J. Cell Sci.* **121**, 255–264 (2008). [doi:10.1242/jcs.006064](https://doi.org/10.1242/jcs.006064) [Medline](#)
16. C. Bonnans, J. Chou, Z. Werb, Remodelling the extracellular matrix in development and disease. *Nat. Rev. Mol. Cell Biol.* **15**, 786–801 (2014). [doi:10.1038/nrm3904](https://doi.org/10.1038/nrm3904) [Medline](#)
17. L. D. Muiznieks, F. W. Keeley, Molecular assembly and mechanical properties of the extracellular matrix: A fibrous protein perspective. *Biochim. Biophys. Acta* **1832**, 866–875 (2013). [doi:10.1016/j.bbadis.2012.11.022](https://doi.org/10.1016/j.bbadis.2012.11.022) [Medline](#)
18. D. Sun, T. C. Jakobs, Structural remodeling of astrocytes in the injured CNS. *Neuroscientist* **18**, 567–588 (2012). [doi:10.1177/1073858411423441](https://doi.org/10.1177/1073858411423441) [Medline](#)
19. S. A. Liddel, B. A. Barres, Reactive astrocytes: Production, function, and therapeutic potential. *Immunity* **46**, 957–967 (2017). [doi:10.1016/j.immuni.2017.06.006](https://doi.org/10.1016/j.immuni.2017.06.006) [Medline](#)
20. K. Pogoda, P. A. Janmey, Glial Tissue Mechanics and Mechanosensing by Glial Cells. *Front. Cell. Neurosci.* **12**, 25 (2018). [doi:10.3389/fncel.2018.00025](https://doi.org/10.3389/fncel.2018.00025) [Medline](#)
21. M. Hara, K. Kobayakawa, Y. Ohkawa, H. Kumamaru, K. Yokota, T. Saito, K. Kijima, S. Yoshizaki, K. Harimaya, Y. Nakashima, S. Okada, Interaction of reactive astrocytes with type I collagen induces astrocytic scar formation through the integrin-N-cadherin pathway after spinal cord injury. *Nat. Med.* **23**, 818–828 (2017). [doi:10.1038/nm.4354](https://doi.org/10.1038/nm.4354) [Medline](#)
22. S. Fedoroff, W. A. McAuley, J. D. Houkle, R. M. Devon, Astrocyte cell lineage. V. Similarity of astrocytes that form in the presence of dBcAMP in cultures to reactive astrocytes in vivo. *J. Neurosci. Res.* **12**, 14–27 (1984). [doi:10.1002/jnr.490120103](https://doi.org/10.1002/jnr.490120103) [Medline](#)
23. V. W. Wu, J. P. Schwartz, Cell culture models for reactive gliosis: New perspectives. *J. Neurosci. Res.* **51**, 675–681 (1998). [doi:10.1002/\(SICI\)1097-4547\(19980315\)51:6<675:AID-JNR2>3.0.CO;2-8](https://doi.org/10.1002/(SICI)1097-4547(19980315)51:6<675:AID-JNR2>3.0.CO;2-8) [Medline](#)
24. S. Robel, B. Berninger, M. Götz, The stem cell potential of glia: Lessons from reactive gliosis. *Nat. Rev. Neurosci.* **12**, 88–104 (2011). [doi:10.1038/nrn2978](https://doi.org/10.1038/nrn2978) [Medline](#)
25. W. S. Sheng, S. Hu, A. Feng, R. B. Rock, Reactive oxygen species from human astrocytes induced functional impairment and oxidative damage. *Neurochem. Res.* **38**, 2148–2159 (2013). [doi:10.1007/s11064-013-1123-z](https://doi.org/10.1007/s11064-013-1123-z) [Medline](#)

26. E. Moeendarbary, I. P. Weber, G. K. Sheridan, D. E. Koser, S. Soleman, B. Haenzi, E. J. Bradbury, J. Fawcett, K. Franze, The soft mechanical signature of glial scars in the central nervous system. *Nat. Commun.* **8**, 14787 (2017). [doi:10.1038/ncomms14787](https://doi.org/10.1038/ncomms14787) [Medline](#)
27. Z. Álvarez, M. A. Mateos-Timoneda, P. Hyroššová, O. Castaño, J. A. Planell, J. C. Perales, E. Engel, S. Alcántara, The effect of the composition of PLA films and lactate release on glial and neuronal maturation and the maintenance of the neuronal progenitor niche. *Biomaterials* **34**, 2221–2233 (2013). [doi:10.1016/j.biomaterials.2012.12.001](https://doi.org/10.1016/j.biomaterials.2012.12.001) [Medline](#)
28. M. Mattotti, Z. Alvarez, J. A. Ortega, J. A. Planell, E. Engel, S. Alcántara, Inducing functional radial glia-like progenitors from cortical astrocyte cultures using micropatterned PMMA. *Biomaterials* **33**, 1759–1770 (2012). [doi:10.1016/j.biomaterials.2011.10.086](https://doi.org/10.1016/j.biomaterials.2011.10.086) [Medline](#)
29. O. S. Lee, S. I. Stupp, G. C. Schatz, Atomistic molecular dynamics simulations of peptide amphiphile self-assembly into cylindrical nanofibers. *J. Am. Chem. Soc.* **133**, 3677–3683 (2011). [doi:10.1021/ja110966y](https://doi.org/10.1021/ja110966y) [Medline](#)
30. T. I. N. G. Li, R. Sknepnek, M. Olvera de la Cruz, Thermally active hybridization drives the crystallization of DNA-functionalized nanoparticles. *J. Am. Chem. Soc.* **135**, 8535–8541 (2013). [doi:10.1021/ja312644h](https://doi.org/10.1021/ja312644h) [Medline](#)
31. W. A. Kibbe, OligoCalc: An online oligonucleotide properties calculator. *Nucleic Acids Res.* **35**, W43–W46 (2007). [doi:10.1093/nar/gkm234](https://doi.org/10.1093/nar/gkm234) [Medline](#)
32. O. S. Lee, V. Cho, G. C. Schatz, Modeling the self-assembly of peptide amphiphiles into fibers using coarse-grained molecular dynamics. *Nano Lett.* **12**, 4907–4913 (2012). [doi:10.1021/nl302487m](https://doi.org/10.1021/nl302487m) [Medline](#)
33. L. Monticelli, S. K. Kandasamy, X. Periolo, R. G. Larson, D. P. Tieleman, S.-J. Marrink, The MARTINI coarse-grained force field: Extension to proteins. *J. Chem. Theory Comput.* **4**, 819–834 (2008). [doi:10.1021/ct700324x](https://doi.org/10.1021/ct700324x) [Medline](#)
34. S. J. Marrink, H. J. Risselada, S. Yefimov, D. P. Tieleman, A. H. de Vries, The MARTINI force field: Coarse grained model for biomolecular simulations. *J. Phys. Chem. B* **111**, 7812–7824 (2007). [doi:10.1021/jp071097f](https://doi.org/10.1021/jp071097f) [Medline](#)